nature nanotechnology

Article

https://doi.org/10.1038/s41565-026-02316-9

Three-dimensional imaging of individual carbon atoms

Received: 14 April 2026

Accepted: 29 September 2026

Published online: 03 November 2026

Check for updates

Na Yeon Kim[1,9], Hanfeng Zhong[1,2,9], Jianhua Zhang[3,9], Colum M. O'Leary[1,9], Yuxuan Liao[1], Ji Zou[4], Haozhi Sha[1], Minh Pham[1], Weiyi Li[1], Yakun Yuan[1], Ji-Hoon Park[5], Dennis S. Kim[6], Huaidong Jiang[3], Jing Kong[5], Miaofang Chi[7,8] & Jianwei Miao[1]

Ptychography is a computational microscopy method that unifies crystallography and microscopy by combining coherent diffraction with iterative phase retrieval. Although multislice electron ptychography achieves deep-sub-ångström lateral resolution, its depth resolution is typically at the nanometre scale. Ptychographic atomic electron tomography (pAET) has enabled three-dimensional (3D) atomic structure determination in nanomaterials, yet reliably resolving individual light atoms remains challenging. Here, using twisted bilayer graphene as a model moiré system, we demonstrate pAET for 3D localization of 6,648 carbon atoms with a precision of 0.12 Å. The resulting 3D atomic structure reveals stacking-dependent interlayer spacing and corrugation across the moiré supercell, as well as chiral lattice distortions with meron-like, anti-meron-like and anti-skyrmion-like textures. Density functional theory calculations based on the experimentally derived structure predict electronic band narrowing and a gap at the K point relative to a relaxed model. Multislice pAET simulations further support extending the method to diamond containing a nitrogen–vacancy centre and to amorphous carbon. These results establish pAET for 3D imaging of individual carbon atoms and open a route to linking 3D atomic structure with the properties of light-element materials.

Determining the three-dimensional (3D) positions of individual atoms is essential for understanding how local structural distortions affect material properties. Scanning probe microscopy is primarily surface-sensitive[1–3], whereas transmission electron microscopy[4–8] and scanning transmission electron microscopy[9–11] generally provide two-dimensional (2D) projection images. Ptychography reconstructs quantitative phase images from coherent diffraction measurements while computationally accounting for probe aberrations[12]. Multislice ptychography extends this approach by modelling wave propagation through successive specimen slices, enabling depth-dependent structure to be recovered without a tilt series or through-focus acquisition[13]. Its depth sensitivity is conceptually and mathematically connected to ankylography[14] through the encoding of 3D information on a curved Ewald sphere[15]. Multislice electron ptychography has revealed depth-dependent structures in both heavy- and light-element materials[16–19], but its depth resolution remains at the nanometre scale

[1]Department of Physics and Astronomy and California NanoSystems Institute, University of California, Los Angeles, Los Angeles, CA, USA. [2]Department of Electrical and Computer Engineering, University of California, Los Angeles, Los Angeles, CA, USA. [3]Center for Transformative Science, ShanghaiTech University, Shanghai, China. [4]Department of Physics, University of Basel, Basel, Switzerland. [5]Department of Electrical Engineering and Computer Science, Massachusetts Institute of Technology, Cambridge, MA, USA. [6]Department of Chemistry and Biochemistry, University of California, Los Angeles, Los Angeles, CA, USA. [7]Center for Nanophase Materials Sciences, Oak Ridge National Laboratory, Oak Ridge, TN, USA. [8]Department of Mechanical Engineering & Materials Science, Duke University, Durham, NC, USA. [9]These authors contributed equally: Na Yeon Kim, Hanfeng Zhong, Jianhua Zhang, Colum M. O'Leary. e-mail: j.miao@ucla.edu

and depends on the probe convergence semi-angle and maximum recorded diffraction angle[14,15,18]. Tilt-coupled multislice electron ptychography achieved approximately 0.9-nm depth resolution using four projections[20]. A single dataset acquired at a 15° specimen tilt, combined with structural constraints and coordinate refinement, also enabled mapping of 3D atomic coordinates in twisted bilayer WSe_2 (ref. 21). Neither study, however, experimentally localized individual light atoms in three dimensions.

To determine 3D atomic structures without relying on crystallinity or averaging over identical structures, atomic electron tomography (AET) has emerged as a leading approach[12,22,23]. Annular dark-field AET has determined individual atomic coordinates with picometre-scale precision in materials containing relatively heavy elements[24–26]. Ptychographic AET (pAET), which combines ptychography with AET, was proposed and validated through numerical simulations[27] and subsequently demonstrated experimentally in oxide nanoparticles and complex nanostructures[28,29]. Extending this capability to individual atoms in light-element materials such as carbon presents a major experimental challenge. Carbon's versatile bonding gives rise to diverse structures, including diamond, graphite, amorphous carbon, fullerenes, carbon nanotubes and graphene[30–32]. In these materials, corrugation, interlayer misalignment, strain, disorder and point defects can alter local bonding environments and structural order, strongly influencing mechanical, thermal, electronic and optical properties[33–36].

Here, we demonstrate pAET for 3D imaging of individual carbon atoms in twisted bilayer graphene (TBG), achieving a 3D precision of 12 pm. Our workflow integrates data acquisition, ptychographic phase retrieval, projection alignment, tomographic reconstruction, iterative atom tracing, coordinate refinement and structural analysis (Extended Data Fig. 1). The resulting atomic model reveals stacking-dependent interlayer spacing and chiral lattice distortions, providing an experimental basis for investigating structure–property relationships in carbon-based materials.

pAET experiment of TBG

We chose TBG as a model system owing to its importance as a quantum material[37] and the necessity to resolve 3D atomic positions for deeper insight into interlayer interactions within moiré patterns[38]. The TBG sample was prepared by stacking graphene monolayers at a small twist angle (Methods). A focused electron probe was used for single-atom fabrication, introducing individual silicon dopants at defect sites in TBG (Supplementary Fig. 1; Methods). The experiment was performed using a 70-keV electron beam, with the TBG sample tilted to 13 different angles using a double-tilt stage (Methods). To minimize vertical vibrations of the freestanding TBG, regions near the edge of the support hole were selected. At each tilt angle, diffraction patterns were recorded by scanning the sample with a 70-keV focused electron probe in a 2D raster pattern (Fig. 1a and Extended Data Table 1). These diffraction patterns encode electron–sample interactions, providing input for computational phase retrieval algorithms that reconstruct the complex functions of both the sample and the probe[12]. By capturing nearly all transmitted and diffracted electrons, ptychography enhances the signal-to-noise ratio and resolution, overcoming the limitations of conventional electron microscopy[39].

Reconstruction was performed using the multimode extended ptychographic iterative engine[40] (ePIE), incorporating four orthogonal probe modes to account for partial coherence and measurement imperfections[41] (Supplementary Fig. 2). To account for the tilt-induced defocus gradient across each projection, the probe was Fresnel-propagated to the local specimen height at each scan position (Methods). The reconstructed phase images of TBG at 13 tilt angles, together with the corresponding annular dark-field images, are shown in Supplementary Figs. 3 and 4 and Supplementary Video 1, where individual silicon dopants are visible and their projected positions appear consistent with the expected tilt geometry across the projections. High-precision tomographic reconstruction required accurate tilt angle calibration, which was achieved using nanoparticles as fiducial markers in low-magnification annular dark-field images (Supplementary Fig. 5), acquired after each ptychography measurement at every tilt angle. The calibrated angles were refined and combined with silicon dopants to align the 13 ptychographic projections (Methods). To ensure consistency, the phase images were scaled to maintain a uniform mean phase value across all projections[42].

After image preprocessing, the 13 ptychographic projections and their calibrated tilt angles were used to reconstruct the 3D atomic structure of TBG (Methods). The reconstruction was performed using the real-space iterative reconstruction (RESIRE) algorithm, and convergence was quantitatively monitored by the *R*-factor[43]. To account for specimen height variations across each tilted view and the resulting depth-dependent probe response, we incorporated a 3D axial probe into the tomographic reconstruction algorithm (Methods). During each iteration, the 3D object was divided into multiple slices along the projection direction, with each slice assigned a defocus-dependent probe. Compared with the simplified parallel-beam approximation, this approach provides a more accurate physical model and improves depth resolution by compensating for defocus variations introduced at different tilt angles (Fig. 1b). From the 3D reconstruction, we selected 863 carbon atoms and averaged their subvolumes to obtain a statistically representative 3D atomic profile. We then fitted the one-dimensional (1D) profile along each axis with a Gaussian plus a constant background and defined the effective resolution as the fitted full width at half maximum above that background. The resulting resolutions were 0.90, 0.80 and 2.86 Å along *x*, *y* and *z*, respectively (Supplementary Fig. 6). The slightly better *y*-axis resolution arises from the graphene lattice orientation, as neighbouring atoms aligned primarily along *x* contribute more to broadening the *x* profile than the *y* profile (Fig. 1e,f). The lower *z*-axis resolution primarily arises from the missing-wedge effect.

By laterally averaging the reconstruction over *x* and *y*, we obtained a 1D intensity profile that revealed two distinct peaks corresponding to the top and bottom graphene layers (Fig. 1b, blue curve). This profile was used to define a 1D support constraint along the *z* axis, modelled as a pair of generalized Gaussian distributions and applied together with the axial probe during tomographic reconstruction. Varying the kernel size of the generalized Gaussian functions yielded consistent 3D reconstructions (Fig. 1c,d). Quantitative analysis showed that, with the 1D *z*-support, the 3D resolutions were 0.89, 0.82 and 1.42 Å along *x*, *y* and *z*, respectively (Extended Data Fig. 2), representing a substantial enhancement along the *z* axis. Figure 1e,f shows the top and bottom layers of TBG, clearly separated following the incorporation of the axial probe and 1D *z*-support constraint into the tomographic reconstruction (Fig. 1g). This separation is further supported by the Fourier transforms of the two layers, which reveal a twist angle of 1.96°, indicating minimal crosstalk between them (Supplementary Fig. 7).

Resolving 3D atomic positions with picometre-level precision

To identify individual atoms with improved precision despite the limited number of tilt angles and the presence of a large missing wedge, we developed an iterative atom-tracing algorithm to extract 3D atomic coordinates from the tomographic reconstruction (Methods). Unlike previous non-iterative approaches[24–26], our algorithm identifies atomic positions iteratively, with tracing errors converging after just a few iterations (Supplementary Fig. 8). The resulting 3D atomic coordinates were further refined using a gradient descent optimization. Each atom was represented by a 3D Gaussian function that accounts for finite spatial resolution, thermal motion and residual experimental broadening. For each experimental projection, calculated projections were generated over a range of tilt angles centred on the calibrated values (Supplementary Fig. 5b). The 3D atomic coordinates, tilt angles and

https://doi.org/10.1038/s41565-026-02316-9

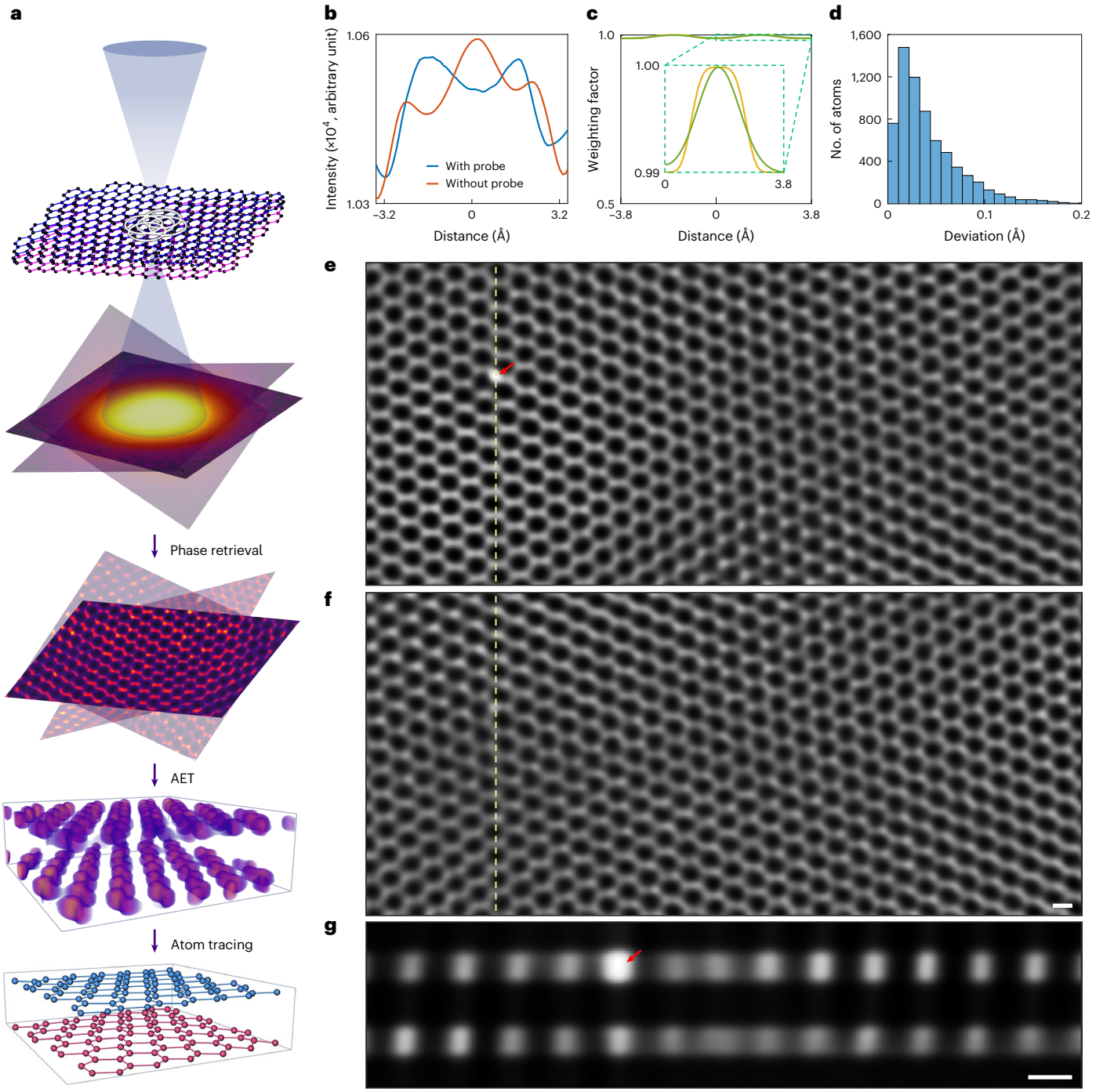


Fig. 1 | Experimental demonstration of pAET for resolving the 3D coordinates of individual carbon atoms in TBG. a, Schematic of the pAET workflow. A focused electron probe scans the sample, producing diffraction patterns that are reconstructed into phase projections. These projections serve as input for tomographic reconstruction, followed by atom tracing and position refinement. **b**, Reconstructed intensity averaged over the entire field of view as a function of z, with and without the 3D axial probe. The two peaks correspond to the top and bottom graphene layers, with clearer separation after incorporation of the axial probe. **c**, Application of a 1D support constraint along the z axis, modelled as a pair of generalized Gaussian distributions with different kernel sizes (yellow and green), iteratively applied to enhance structural precision. **d**, Comparison of atomic coordinates obtained using different z-support kernel sizes, yielding a 3D RMSD of 5 pm. **e**,**f**, Cropped top (**e**) and bottom (**f**) graphene layers resolved after applying both the 3D axial probe kernel and the 1D support constraint. Red arrows indicate silicon dopants. **g**, Side view of both layers along the dashed lines indicated in (**e**) and (**f**), confirming effective layer separation. Scale bars, 2 Å.

projection alignment were iteratively refined by minimizing the difference between the experimental and calculated projections (Methods). The aligned projections and refined tilt angles were then used for the final tomographic reconstruction with the axial probe and 1D z-support, followed by iterative atom tracing and coordinate refinement to obtain the final 3D atomic model.

To estimate the 3D precision of pAET, we generated 13 multislice ptychographic datasets from the experimental 3D atomic model using the refined tilt angles and the same data-acquisition parameters as in the experiment (Extended Data Table 1; Methods). Thermal vibrations were modelled with 64 frozen-phonon configurations, and Poisson noise was added at the experimental dose. The datasets

https://doi.org/10.1038/s41565-026-02316-9

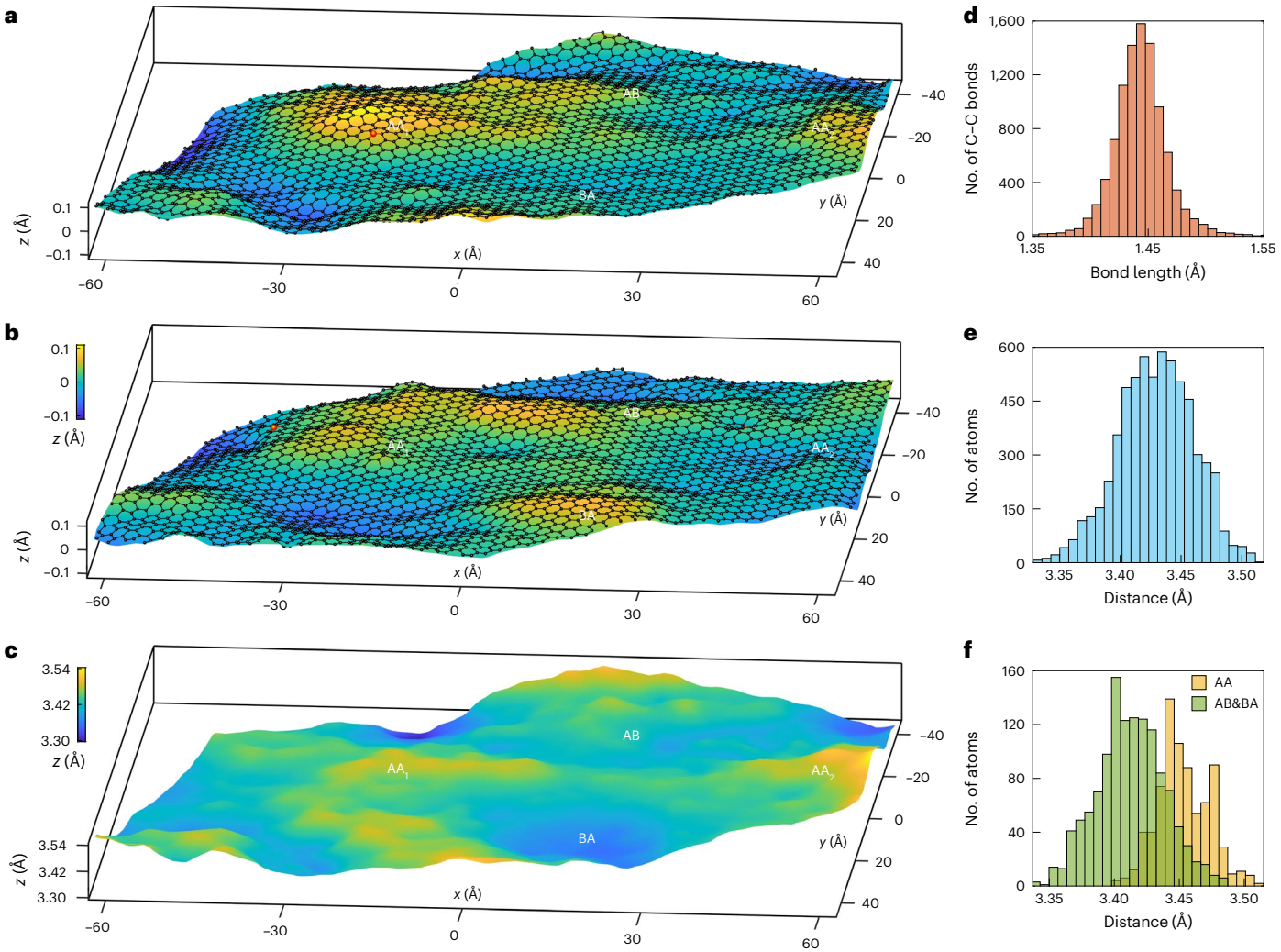


Fig. 2 | Three-dimensional atomic corrugations in TBG arising from stacking-dependent interlayer interactions. a,**b**, Out-of-plane corrugations in the top (**a**) and bottom (**b**) graphene layers of the experimental 3D atomic model obtained using the full pAET workflow. **c**, Spatial variation of the interlayer spacing, revealing stacking-dependent corrugation across AA, AB and BA regions. To improve displacement-field precision at the expense of resolution, atomic positions were convolved with a 3D Gaussian kernel with standard deviations of 1.26 Å in x and y (half the in-plane lattice constant) and 1.71 Å in z (half the mean interlayer spacing). **d**, Histogram of sp^2 C–C bond lengths, with a mean of 1.44 ± 0.02 Å. **e**, Histogram of the interlayer spacing, with a mean of 3.43 ± 0.03 Å. **f**, Interlayer spacing distributions in AA and AB/BA stacking regions, with mean values of 3.45 ± 0.02 Å and 3.41 ± 0.03 Å, respectively. Values are reported as mean ± s.d.; because the interlayer spacing is averaged over many atom pairs, the uncertainty in the mean value is substantially smaller than the positional uncertainty of individual atoms.

were reconstructed using multimode ePIE[40,41]. To reproduce residual broadening from partial coherence and other experimental effects, each reconstructed phase projection was convolved with a Gaussian kernel whose width was optimized against the corresponding experimental projection. The 13 simulated projections were then processed through the same pAET workflow used for the experimental data, yielding a validation atomic model. Comparison with the input experimental model yielded root-mean-square deviations (RMSDs) of 6, 5 and 7 pm along x, y and z, respectively, and an overall 3D RMSD of 11 pm (Extended Data Fig. 3). An independent randomized ground-truth test gave corresponding RMSDs of 4, 5 and 8 pm and a consistent overall 3D RMSD of 10 pm (Methods; Supplementary Fig. 9).

To further assess the 3D precision of pAET directly from the experimental data, we performed two independent analyses. First, we replaced the generalized Gaussian support with two transient square supports along the z axis, each 1.52 Å wide and centred on one graphene layer (Supplementary Fig. 10a), substantially broader than any plausible local out-of-plane variation. The supports were applied only during the first 50 of 200 iterations and then removed. The atomic coordinates were subsequently refined against the experimental projections without any support constraint. The resulting model closely agreed with the generalized-Gaussian-support model, with an overall RMSD of 8 pm (Supplementary Fig. 10b). Second, we reconstructed the same 13 projections without either the 1D z-support or the axial probe. The two graphene layers remained resolved, allowing atoms in each layer to be traced independently and used to initialize a flat-bilayer model. The 3D coordinates were then refined against the experimental projections without either constraint, producing a 3D atomic model that matched the full pAET model, with an overall RMSD of 12 pm (Extended Data Fig. 4). These independent analyses support a 3D precision of 12 pm for the full pAET workflow. The consistency among the models reflects the final refinement of each coordinate set against the same experimental projections, which reduces sensitivity to the initial model.

Figure 2a–c shows the top and bottom graphene layers and the corresponding interlayer spacing of the experimental 3D atomic model, comprising 6,648 carbon atoms and three silicon dopants with one identified carbon vacancy. Yellow and blue regions represent upward

https://doi.org/10.1038/s41565-026-02316-9

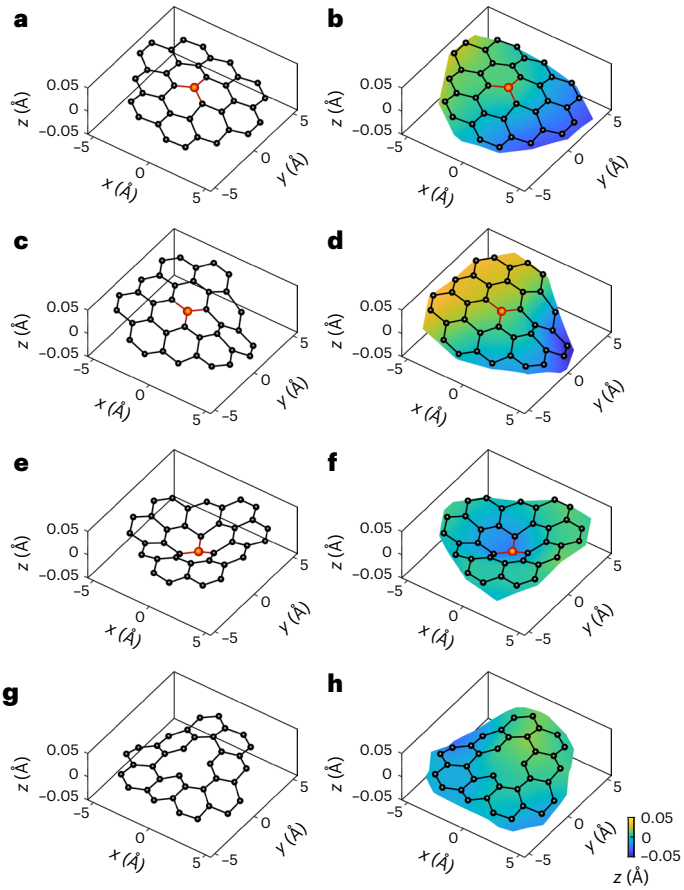


Fig. 3 | Local 3D structures of three Si dopants and one carbon vacancy in TBG. a–**d**, Two Si dopants in the top (**a** and **b**) and bottom (**c** and **d**) graphene layers, each showing small local distortion. **e**,**f**, Third Si dopant in the bottom layer, exhibiting pronounced local lattice distortion. **g**,**h**, Carbon vacancy in the bottom layer, showing small local distortion. **a**, **c**, **e** and **g** show the atomic coordinates, while **b**, **d**, **f** and **h** show the corresponding coordinates overlaid with a colour map representing the local z-coordinate deviation. Si atoms are shown in orange.

and downward atomic corrugations, respectively, while black lines indicate sp^2 C–C bonds. The bond length was determined to be 1.44 ± 0.02 Å (mean ± s.d.; Fig. 2d), closely matching the value of 1.43 Å in the density functional theory (DFT)-relaxed model (Supplementary Fig. 11). The experimental 3D atomic model also reveals the local environments of the three Si dopants and one carbon vacancy (Fig. 3). Two Si dopants, one in each graphene layer, show small local distortions (Fig. 3a–d), whereas the third dopant in the bottom layer is associated with pronounced distortion of the surrounding lattice (Fig. 3e,f). The carbon vacancy, also located in the bottom layer, shows small local distortion (Fig. 3g,h). The contrasting Si environments reveal site-dependent variations in the local lattice geometry, demonstrating the ability of pAET to characterize individual defects and their surrounding 3D atomic structures in TBG.

At the moiré scale, the experimentally determined 3D coordinates enable quantitative analysis of interlayer spacing across different local stacking configurations. The interlayer distance in the experimental model is 3.43 ± 0.03 Å, consistent with the DFT-relaxed model value of 3.41 ± 0.04 Å (Fig. 2e and Supplementary Fig. 11e). However, a closer comparison reveals stacking-dependent differences. The experimental interlayer spacings are 3.45 ± 0.02 Å in AA regions and 3.41 ± 0.03 Å in AB/BA regions (Fig. 2f), compared with 3.49 ± 0.01 Å and 3.37 ± 0.01 Å, respectively, in the DFT-relaxed model (Supplementary Fig. 11f). The experimental distributions are broader for each stacking configuration, with a smaller separation between the AA and AB/BA mean spacings. Structural heterogeneity is also evident between the AA regions. Both layers curve upward in AA_1, whereas AA_2 exhibits a pronounced bulging deformation (Fig. 2a–c). Such sample-specific corrugations can induce charge redistribution, break local rotational symmetry and modify the electronic structure of TBG[8,44].

Quantifying 3D chiral lattice distortions in TBG

Using the experimental 3D atomic model, we quantitatively analysed 3D displacement vectors in TBG, which represents a substantial advancement over previous experimental efforts limited to 2D characterization[45,46]. To enhance the statistical precision of the displacement vector field, the atomic positions were convolved with a 3D Gaussian kernel whose standard deviations corresponded to the in-plane lattice constant and the mean interlayer spacing along the *z* axis. This smoothing suppresses high-frequency noise and local fluctuations, enabling more robust extraction of long-wavelength structural distortions. To investigate the displacement field driven by van der Waals interactions, we compared the experimental 3D atomic model with an unrelaxed TBG model composed of two flat graphene layers (Methods). This comparison enabled extraction of 3D displacement vectors for both the top and bottom layers (Fig. 4a,b). The displacement vectors show strong in-plane vorticity around the AA stacking regions, accompanied by out-of-plane components along the *z* axis, which exhibit chiral lattice distortions resembling magnetic merons and skyrmions[47].

We quantified these chiral textures by calculating their skyrmion numbers (Methods). The experimental TBG model contains two meron-like, three anti-meron-like and one anti-skyrmion-like structural texture. Figure 4c,d illustrates the 3D displacement vector fields of meron-like and anti-meron-like structural textures, both featuring elliptical geometries with skyrmion numbers of −0.42 and 0.46, respectively. Additional meron-like and anti-meron-like structural textures are shown in Extended Data Fig. 5. The displacement vectors are oriented along the *z* axis near the core, with their polar angles gradually increasing outwards, tilting predominantly into the *xy* plane at the boundary. The experimentally observed vector fields deviate from those in the DFT-relaxed TBG model, which display perfectly symmetric meron-like and anti-meron-like structural textures with skyrmion numbers of −0.5 and +0.5, respectively (Supplementary Fig. 12a,b). Figure 4e shows the 3D displacement vector field of an anti-skyrmion-like structural texture, characterized by an elliptical geometry and a skyrmion number of 0.97. This configuration features an anti-meron-like core (Fig. 4d), with some boundary vectors tilting their polar angles close to 180°. Compared with its counterpart in the DFT-relaxed model (Supplementary Fig. 12c), the experimental anti-skyrmion-like structural texture exhibits deviations in geometry, skyrmion number and 3D displacement-field configuration.

To assess the robustness of the chiral lattice distortions observed in TBG, we repeated the analysis after halving the Gaussian kernel standard deviations along the *x*, *y* and *z* axes. Although the smaller kernel increases local fluctuations, the main features of the 3D displacement vector field and the associated chiral lattice distortions remained unchanged (Fig. 4 and Extended Data Fig. 6). The same six chiral textures, two meron-like, three anti-meron-like and one anti-skyrmion-like, were identified using both kernel sizes. We further assessed reproducibility through a split-half analysis of the raw experimental data. At each of the 13 tilts, the ptychographic scan positions were divided into two interleaved half-datasets and independently processed through the complete pAET workflow. The resulting displacement fields showed minor local differences but preserved the same overall chiral distortions (Extended Data Fig. 7). Consistent displacement fields were also recovered from an experimental 3D atomic model obtained without the 1D *z*-support or axial-probe constraint (Supplementary Fig. 13). These tests show that the observed textures are robust to kernel size, data splitting and reconstruction constraints.

https://doi.org/10.1038/s41565-026-02316-9

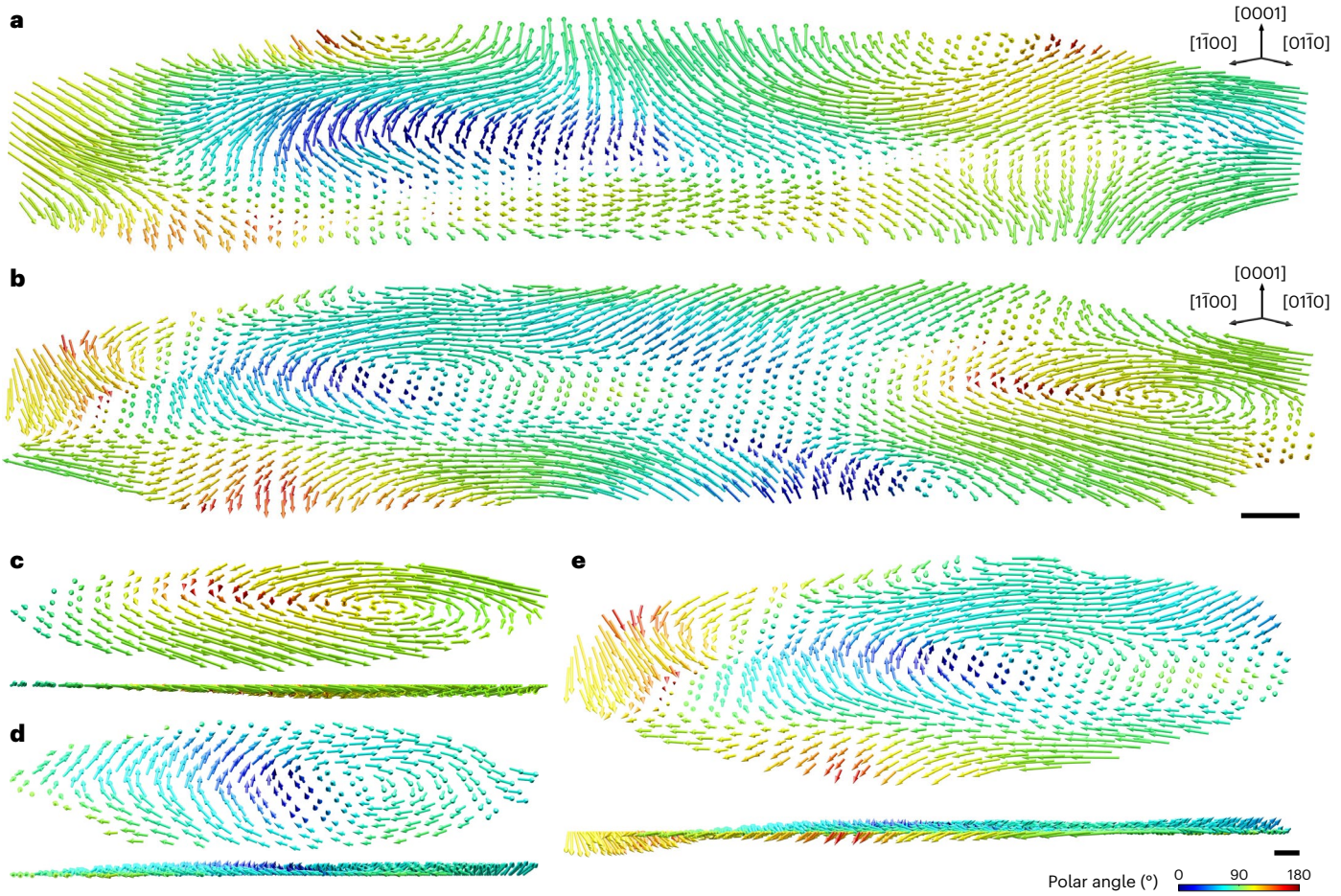


Fig. 4 | Quantification of 3D displacement vectors and chiral lattice distortions in experimental TBG. a,**b**, Three-dimensional displacement vector fields in the top (**a**) and bottom (**b**) graphene layers. Vector colour represents the polar angle measured from the +*z* axis. **c**,**d**, Localized 3D vector fields of meron-like (**c**) and anti-meron-like (**d**) structural textures. Near the core, vectors align with the *z* axis and gradually tilt into the *xy* plane towards the boundaries, characteristic of chiral lattice distortions. **e**, The 3D vector field of an anti-skyrmion-like structural texture incorporating the anti-meron-like core from **d**. Several boundary vectors approach polar angles near 180°, indicating more complex out-of-plane deformation. To improve displacement-field precision at the expense of spatial resolution, atomic positions were convolved with a 3D Gaussian kernel with standard deviations of 2.51 Å in *x* and *y* (the in-plane lattice constant) and 3.43 Å in *z* (the mean interlayer spacing). Displacement vectors are plotted on the same spatial scale as the atomic structure, with their lengths enlarged 25-fold for visualization. Scale bars, 5 Å (**b**) and 2 Å (**e**), corresponding to actual displacement magnitudes of 20 pm and 8 pm, respectively.

DFT analysis and pAET simulations of carbon materials

Building on this structural analysis, we investigated how chiral lattice distortions affect the electronic properties of TBG by incorporating experimentally determined 3D atomic coordinates into DFT calculations. Although DFT has been widely used to predict TBG's electronic properties[48], it typically relies on idealized lattice models with manually introduced defects, which are then relaxed to their ground-state configurations. By incorporating experimentally measured atomic coordinates, our approach captures the sample-specific structural complexity of real TBG and enables direct evaluation of its electronic structure. Because DFT calculations using the unsmoothed 3,268-atom experimental model did not converge reliably, we smoothed the atomic coordinates with a 3D Gaussian kernel with standard deviations of 1.26 Å along *x* and *y* and 1.71 Å along *z*, adjusting only atoms near the supercell boundary to maintain periodic continuity (Methods). This procedure suppressed high-frequency positional noise while preserving the moiré-scale structure. Figure 5a shows a moiré supercell containing 3,267 carbon atoms and a silicon dopant, including two anti-meron-like structural textures. Compared with the DFT-relaxed model, the experimental 3D atomic coordinates exhibit larger out-of-plane variations along the *z* axis (Fig. 5b,c).

Figure 5d compares the electronic band structures calculated from the experimentally derived and DFT-relaxed models. In the relaxed model (green), the valence and conduction bands meet at the K point near the Fermi level, forming a gapless Dirac cone consistent with semimetallic behaviour, analogous to monolayer graphene[49]. By contrast, the experimentally derived model (blue) exhibits a 22-meV gap between these bands at K. Replacing the single Si atom with carbon produced essentially unchanged low-energy bands and K-point gap, showing that these features persist without the Si dopant (Supplementary Fig. 14). At room temperature, the thermal energy (~26 meV) is comparable to the calculated 22 meV gap at K, suggesting appreciable thermal excitation across this energy scale. Upon cooling, thermal excitation near K is expected to decrease, potentially leading to more insulating behaviour if the Fermi level lies within a global band gap. In addition, relative to the DFT-relaxed model, the experimentally derived structure raises the valence-band energy and lowers the conduction-band energy at the Γ point, resulting in a bandwidth reduction of up to 13.5%. This narrowing is consistent with stronger interlayer electronic coupling associated with the sample-specific corrugation and stacking distortions.

To examine whether pAET can be extended to thicker and structurally disordered carbon materials, we performed two multislice simulations under realistic noise and electron dose conditions (Methods). First, we simulated a 15-nm diamond nanocrystal containing a

https://doi.org/10.1038/s41565-026-02316-9

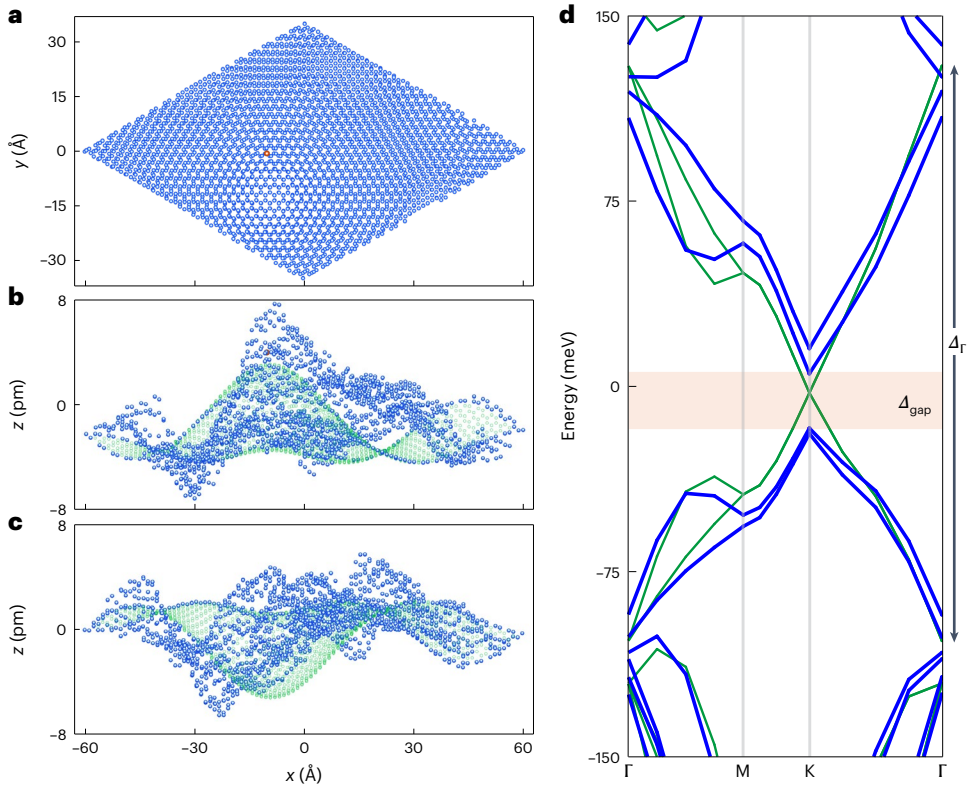


Fig. 5 | Comparison of electronic band structures in TBG from experimental and DFT-relaxed atomic models. a, Experimental 3D atomic structure of a moiré supercell containing 3,267 carbon atoms and one silicon dopant (red dot), including two anti-meron-like features. **b**,**c**, Overlay of atomic positions from the experimental (blue) and DFT-relaxed (green) models in the top (**b**) and bottom (**c**) graphene layers, showing deviations of the experimental structure from the relaxed model. **d**, Electronic band structures computed from the two models. The experimental model (blue) exhibits an asymmetric band structure with a 22-meV gap at the K point and a bandwidth reduction of up to 13.5% at the Γ point. The DFT-relaxed model (green) retains a symmetric band structure with a gapless Dirac cone.

nitrogen–vacancy (NV) centre using 57 tilt angles from −70° to 70°, reflecting the larger number of projections required for thicker specimens at a given target resolution. Because the crystal thickness was about three times the probe depth of focus, single-slice pAET could not resolve individual atoms in the final 3D reconstruction. Multislice pAET performed substantially better, resolving the individual carbon atoms and the vacancy at the NV centre, while incorporation of the depth-dependent probe response improved the 3D localization precision from 9 pm to 7 pm (Extended Data Fig. 8). Second, we simulated a 5-nm amorphous carbon nanoparticle containing 7,514 atoms using 37 ptychographic projections. Multislice pAET identified 99% of the atoms and recovered the 3D coordinates with an overall RMSD of 11 pm. The reconstructed model also reproduced the medium-range-order ring structures of the ground-truth model (Extended Data Fig. 9). These results demonstrate the broader potential of pAET for high-precision 3D atomic structure determination in both crystalline materials containing defects and disordered materials.

Conclusion

We demonstrate that pAET achieves picometre-precision determination of the 3D coordinates of individual carbon atoms in TBG, revealing interlayer spacing variations governed by local stacking. Quantitative analysis of the 3D displacement vector field reveals van der Waals-driven chiral lattice distortions, including meron-like, anti-meron-like and anti-skyrmion-like structural textures. Incorporating the experimentally determined 3D atomic coordinates into DFT calculations predicts an asymmetric electronic band structure with a 22-meV gap at K, in contrast to the gapless Dirac cone predicted by the DFT-relaxed model. Beyond TBG, multislice pAET simulations further support the broader applicability of the method, including resolving an NV centre embedded deep within a 15-nm diamond crystal and determining the 3D atomic structure of a 5-nm amorphous carbon nanoparticle. Continued methodological advances could enable pAET to achieve sub-ångström 3D imaging across a wide range of low-Z materials, including van der Waals heterostructures[38], quantum emitters[35], superconductors[1,19], charge-density-wave systems[50], ferroelectrics[51], catalysts[52] and amorphous carbon[32], thereby providing atomic-scale insight into structure–function relationships in complex and beam-sensitive materials.

Online content

Any methods, additional references, Nature Portfolio reporting summaries, source data, extended data, supplementary information, acknowledgements, peer review information; details of author contributions and competing interests; and statements of data and code availability are available at https://doi.org/10.1038/s41565-026-02316-9.

References

1. Oh, M. et al. Evidence for unconventional superconductivity in twisted bilayer graphene. *Nature* **600**, 240–245 (2021).
2. Jiang, Y. et al. Charge order and broken rotational symmetry in magic-angle twisted bilayer graphene. *Nature* **573**, 91–95 (2019).
3. McGilly, L. J. et al. Visualization of moiré superlattices. *Nat. Nanotechnol.* **15**, 580–584 (2020).
4. Hashimoto, A., Suenaga, K., Gloter, A., Urita, K. & Iijima, S. Direct evidence for atomic defects in graphene layers. *Nature* **430**, 870–873 (2004).

5. Gómez-Navarro, C. et al. Atomic structure of reduced graphene oxide. *Nano Lett.* **10**, 1144–1148 (2010).
6. Meyer, J. C. et al. Experimental analysis of charge redistribution due to chemical bonding by high-resolution transmission electron microscopy. *Nat. Mater.* **10**, 209–215 (2011).
7. Warner, J. H. et al. Dislocation-driven deformations in graphene. *Science* **337**, 209–212 (2012).
8. Yoo, H. et al. Atomic and electronic reconstruction at the van der Waals interface in twisted bilayer graphene. *Nat. Mater.* **18**, 448–453 (2019).
9. Suenaga, K. & Koshino, M. Atom-by-atom spectroscopy at graphene edge. *Nature* **468**, 1088–1090 (2010).
10. Li, Y. et al. An oxygen reduction electrocatalyst based on carbon nanotube–graphene complexes. *Nat. Nanotechnol.* **7**, 394–400 (2012).
11. Krivanek, O. L. et al. Atom-by-atom structural and chemical analysis by annular dark-field electron microscopy. *Nature* **464**, 571–574 (2010).
12. Miao, J. Computational microscopy with coherent diffractive imaging and ptychography. *Nature* **637**, 281–295 (2025).
13. Maiden, A. M., Humphry, M. J. & Rodenburg, J. M. Ptychographic transmission microscopy in three dimensions using a multi-slice approach. *J. Opt. Soc. Am. A* **29**, 1606–1614 (2012).
14. Raines, K. S. et al. Three-dimensional structure determination from a single view. *Nature* **463**, 214–217 (2010).
15. Suzuki, A. et al. High-resolution multislice X-ray ptychography of extended thick objects. *Phys. Rev. Lett.* **112**, 053903 (2014).
16. Gao, S. et al. Electron ptychographic microscopy for three-dimensional imaging. *Nat. Commun.* **8**, 163 (2017).
17. Chen, Z. et al. Electron ptychography achieves atomic-resolution limits set by lattice vibrations. *Science* **372**, 826–831 (2021).
18. O'Leary, C. M. et al. Three-dimensional structure of buried heterointerfaces revealed by multislice ptychography. *Phys. Rev. Appl.* **22**, 014016 (2024).
19. Dong, Z. et al. Visualization of oxygen vacancies and self-doped ligand holes in $La_3Ni_2O_{7-\delta}$. *Nature* **630**, 847–852 (2024).
20. Dong, Z. et al. Sub-nanometer depth resolution and single dopant visualization achieved by tilt-coupled multislice electron ptychography. *Nat. Commun.* **16**, 1219 (2025).
21. Huang, J. et al. 3D mapping of defects and moiré corrugations via electron ptychography atomic coordinate retrieval. *Sci. Adv.* **12**, eaeb4305 (2026).
22. Miao, J., Ercius, P. & Billinge, S. J. L. Atomic electron tomography: 3D structures without crystals. *Science* **353**, aaf2157 (2016).
23. Liao, Y. et al. Accurate determination of the 3D atomic structure of amorphous materials. *Nature* **649**, 1123–1129 https://doi.org/10.1038/s41586-025-09857-4 (2026).
24. Yang, Y. et al. Deciphering chemical order/disorder and material properties at the single-atom level. *Nature* **542**, 75–79 (2017).
25. Tian, X. et al. Correlating the three-dimensional atomic defects and electronic properties of two-dimensional transition metal dichalcogenides. *Nat. Mater.* **19**, 867–873 (2020).
26. Yang, Y. et al. Determining the three-dimensional atomic structure of an amorphous solid. *Nature* **592**, 60–64 (2021).
27. Chang, D. J. et al. Ptychographic atomic electron tomography: towards three-dimensional imaging of individual light atoms in materials. *Phys. Rev. B* **102**, 174101 (2020).
28. Pelz, P. M. et al. Solving complex nanostructures with ptychographic atomic electron tomography. *Nat. Commun.* **14**, 7906 (2023).
29. Romanov, A., Cho, M. G., Scott, M. C. & Pelz, P. M. Multi-slice electron ptychographic tomography for three-dimensional phase-contrast microscopy beyond the depth of focus limits. *J. Phys. Mater.* **8**, 015005 (2025).
30. Georgakilas, V., Perman, J. A., Tucek, J. & Zboril, R. Broad family of carbon nanoallotropes: classification, chemistry, and applications of fullerenes, carbon dots, nanotubes, graphene, nanodiamonds, and combined superstructures. *Chem. Rev.* **115**, 4744–4822 (2015).
31. Geim, A. K. & Novoselov, K. S. The rise of graphene. *Nat. Mater.* **6**, 183–191 (2007).
32. Robertson, J. Diamond-like amorphous carbon. *Mater. Sci. Eng R* **37**, 129–281 (2002).
33. Coleman, J. N., Khan, U., Blau, W. J. & Gun'ko, Y. K. Small but strong: a review of the mechanical properties of carbon nanotube-polymer composites. *Carbon* **44**, 1624–1652 (2006).
34. Balandin, A. A. Thermal properties of graphene and nanostructured carbon materials. *Nat. Mater.* **10**, 569–581 (2011).
35. Aharonovich, I., Englund, D. & Toth, M. Solid-state single-photon emitters. *Nat. Photon.* **10**, 631–641 (2016).
36. Charlier, J.-C. Defects in carbon nanotubes. *Acc. Chem. Res.* **35**, 1063–1069 (2002).
37. Andrei, E. Y. & MacDonald, A. H. Graphene bilayers with a twist. *Nat. Mater.* **19**, 1265–1275 (2020).
38. Novoselov, K. S., Mishchenko, A., Carvalho, A. & Castro Neto, A. H. 2D materials and van der Waals heterostructures. *Science* **353**, aac9439 (2016).
39. Jiang, Y. et al. Electron ptychography of 2D materials to deep sub-ångström resolution. *Nature* **559**, 343–349 (2018).
40. Maiden, A. M. & Rodenburg, J. M. An improved ptychographical phase retrieval algorithm for diffractive imaging. *Ultramicroscopy* **109**, 1256–1262 (2009).
41. Chen, Z. et al. Mixed-state electron ptychography enables sub-angstrom resolution imaging with picometer precision at low dose. *Nat. Commun.* **11**, 2994 (2020).
42. Guizar-Sicairos, M. et al. Phase tomography from x-ray coherent diffractive imaging projections. *Opt. Express* **19**, 21345–21357 (2011).
43. Pham, M., Yuan, Y., Rana, A., Osher, S. & Miao, J. Accurate real space iterative reconstruction (RESIRE) algorithm for tomography. *Sci. Rep.* **13**, 5624 (2023).
44. Ohta, T., Bostwick, A., Seyller, T., Horn, K. & Rotenberg, E. Controlling the electronic structure of bilayer graphene. *Science* **313**, 951–954 (2006).
45. Kazmierczak, N. P. et al. Strain fields in twisted bilayer graphene. *Nat. Mater.* **20**, 956–963 (2021).
46. Sung, S. H. et al. Torsional periodic lattice distortions and diffraction of twisted 2D materials. *Nat. Commun.* **13**, 7826 (2022).
47. Yu, X. Z. et al. Transformation between meron and skyrmion topological spin textures in a chiral magnet. *Nature* **564**, 95–98 (2018).
48. Carr, S., Fang, S. & Kaxiras, E. Electronic-structure methods for twisted moiré layers. *Nat. Rev. Mater.* **5**, 748–763 (2020).
49. Castro Neto, A. H., Guinea, F., Peres, N. M. R., Novoselov, K. S. & Geim, A. K. The electronic properties of graphene. *Rev. Mod. Phys.* **81**, 109–162 (2009).
50. Grüner, G. The dynamics of charge-density waves. *Rev. Mod. Phys.* **60**, 1129–1181 (1988).
51. Scott, J. F. Applications of modern ferroelectrics. *Science* **315**, 954–959 (2007).
52. Yang, Y. et al. Atomic-scale identification of active sites of oxygen reduction nanocatalysts. *Nat. Catal.* **7**, 796–806 (2024).

Publisher's note Springer Nature remains neutral with regard to jurisdictional claims in published maps and institutional affiliations.

Springer Nature or its licensor (e.g. a society or other partner) holds exclusive rights to this article under a publishing agreement with the author(s) or other rightsholder(s); author self-archiving of the accepted manuscript version of this article is solely governed by the terms of such publishing agreement and applicable law.

© The Author(s), under exclusive licence to Springer Nature Limited 2026

Methods

TBG synthesis

Monolayer graphene was synthesized via chemical vapour deposition[53] on a 25-µm-thick Cu foil (Alfa Aesar, 99.8%, #13382). The chemical vapour deposition-grown graphene was spin-coated with poly(methyl methacrylate) (PMMA), followed by selective etching of the Cu foil using ferric chloride solution (CE-100, Transene). The graphene/PMMA layer was rinsed multiple times in deionized water to remove Cu etchant residues and transferred onto a transmission electron microscopy sample grid (Quantifoil 200 mesh Au R 1.2/1.3). After air drying, the grid was heated to 90 °C to improve adhesion between the graphene/PMMA layer and the grid. The PMMA layer was then removed by soaking in a 60 °C acetone bath, and the graphene/grid was rinsed in isopropyl alcohol. To eliminate volatile organics, the grid was annealed under Ar/H_2 gas (300 sccm/100 sccm) at 350 °C for 3 h. A second graphene layer was transferred onto the grid using the same procedure, resulting in TBG. To minimize electron-beam-induced amorphous carbon contamination during data collection, UVO treatment (Zone-TEM, Hitachi) was applied to both sides of the sample grid for 5 min. Finally, the sample and holder stage were annealed in vacuum (10^{-3} Pa, 160 °C) for 18 h to remove volatile compounds before data acquisition.

Electron beam manipulation of individual dopant atoms

To incorporate individual silicon dopants into TBG lattices, a 100-keV converged electron beam was raster-scanned over regions of TBG enriched with dopant sources (Supplementary Fig. 1). The incident electrons, exceeding the carbon knock-on threshold energy[54], created atomic vacancies in the TBG lattice. Subsequently, the electron beam was precisely applied in line-profile scanning to transfer source atoms from impurity-rich areas to these defect sites. The Si dopants were incorporated into substitutional sites in the graphene lattice.

Ptychography data acquisition

Electron ptychography data were collected on a Nion UltraSTEM 100 scanning transmission electron microscope equipped with an optically coupled Hamamatsu Orca CMOS detector (2,048 × 2,048 pixels) and a double-tilt side-entry holder. The holder provided two orthogonal tilt axes, each with a nominal range of ±22°. The detector was windowed to 48 × 48 pixels with a dwell time of 1.5 ms per probe position. An accelerating voltage of 70 kV was used to minimize knock-on damage to carbon, and a convergence semi-angle of 32 mrad was selected to achieve atomic resolution with high contrast. To optimize the imaging conditions, we performed preliminary tests and found that a focused probe yielded slightly better reconstruction quality for our specific set-up. A probe current of 60 pA and a scan step size of 0.65 Å were used, yielding 230 × 230 diffraction patterns over the TBG region of interest. The electron dose per tilt was 1.3×10^6 e^- $Å^{-2}$, giving a total dose of 1.69×10^7 e^- $Å^{-2}$, which is below the threshold for defect formation in graphene[55]. Data acquisition was repeated at 13 tilt angles using the double-tilt holder, with the specific angles listed in Supplementary Fig. 5b. To mitigate beam effects during acquisition, we introduced ~1-h intervals between tilts to allow thermal and mechanical relaxation and to reduce holder hysteresis. Beam blanking was applied between scans, and dwell times were minimized to limit radiolysis and contamination.

Ptychographic reconstruction and image preprocessing

Each TBG projection was reconstructed using a customized multimode ePIE algorithm[40]. Diffraction patterns were zero-padded to 192 × 192 pixels, yielding a real-space pixel size of 0.095 Å. This step was used solely to refine the computational sampling grid and reduce discretization error. To account for partial coherence, four orthogonal probe modes were used in the reconstruction[41,56] (Supplementary Fig. 2). Robustness was evaluated by repeating the reconstructions with two, four and six modes, with and without a detector response model; results with four or more modes were highly consistent and insensitive to the detector model. Both single- and multislice ptychographic reconstructions produced very similar results because the local beam path through the bilayer remained much smaller than the ~4.3-nm probe depth of focus at all tilt angles. To compensate for the lateral defocus gradient across each tilted projection, the probe at every scan position was assigned the defocus predicted by the specimen geometry and Fresnel-propagated along the optical axis. Supplementary Fig. 3 shows the 13 ptychographic phase images across the tilt series. Phase images were aligned using the centre-of-mass method[57], with Si substitutional dopants providing supplementary positional references.

Angle calibration

The nominal angles were measured using the Nion double-tilt holder during data acquisition but required calibration to account for stage hysteresis. To calibrate the angles, we utilized low-magnification annular dark-field images featuring multiple metal nanoparticles. The x and y coordinates of each nanoparticle were determined through 2D Gaussian fitting. The tilt angles of the 13 projections were calibrated using the least-squares method, minimizing the error function E,

$$E = \sum_i \sum_j \left\{ \left[P_x\left(r_i, \psi_j, \theta_j\right) - x_i^j \right]^2 + \left[P_y\left(r_i, \psi_j, \theta_j\right) - y_i^j \right]^2 \right\}, \quad (1)$$

where P_x and P_y are the functions projecting the 3D coordinates of nanoparticles onto the x and y coordinates, respectively. r_i denotes the 3D coordinates of the ith nanoparticle, while ψ_j and θ_j are the tilt angles for the jth projection. The measured x and y coordinates for the ith particle in the jth projection are given by x_i^j and y_i^j. Using equation (1), we jointly determined the 3D coordinates of all nanoparticles within the field of view and the projection orientations across the complete tilt series, yielding the calibrated tilt angles and tilt axes shown in Supplementary Fig. 5. The least-squares optimization converged to consistent solutions from different initial guesses.

Tomographic reconstruction incorporating a 3D axial probe kernel

The pre-processed dataset was used as input to an enhanced version of the RESIRE algorithm[43]. This algorithm minimizes the least-squares difference between the measured ptychographic projections and projections calculated from the 3D object. To account for the probe's depth dependence, we incorporated a depth-dependent axial probe kernel into the loss function for each calibrated projection orientation, $\omega = (\phi, \theta, \psi)$,

$$\varepsilon_\omega(O) = \frac{1}{2} \sum_{x,y} \left| \sum_z K(z) * O_\omega\{x,y,z\} - b_\omega\{x,y\} \right|^2 \quad (2)$$

where * denotes the convolution operator, $O_\omega\{x,y,z\}$ is the 3D object $O\{x,y,z\}$ rotated to the orientation ω, $K(z)$ is the axial probe kernel corresponding to depth z, and b_ω is the measured projection at the calibrated orientation shown in Supplementary Fig. 5. The axial probe kernel was defined from the experimental probe parameters (electron voltage and convergence semi-angle) and positioned relative to the sample according to the measured defocus. Because the projection operators in equation (2) are linear, we solved the minimization problem using gradient descent. Quantitative simulations demonstrated that this kernel produced reconstructions of higher fidelity than those obtained with either the parallel-beam assumption or a more complex probe function extracted from ptychographic reconstructions. In the tomographic reconstruction of our experimental data, the number of slices varied with the tilt angle: higher tilt angles required more slices, while lower tilt angles required fewer. For the 13 projections, we used between 5 and 15 slices, with each slice having a thickness of 80 pixels (7.6 Å). Reconstructions performed with different slice thicknesses

yielded consistent atomic coordinates, confirming that the results are robust to the choice of slice sampling.

For the 13 experimental projections, we performed three iterative RESIRE reconstruction cycles. The first cycle consisted of 80 iterations and produced a preliminary 3D volume. We then averaged this volume laterally over the x and y directions to obtain a 1D intensity profile along z, which showed two peaks corresponding to the two graphene layers (Fig. 1b). The peak positions defined the centres of two generalized Gaussian functions, while the peak widths guided their respective widths. These functions formed the 1D z-support used in the subsequent reconstruction cycles. We tested different Gaussian kernel widths to evaluate the robustness of the reconstruction (Fig. 1c,d). Next, RESIRE was run for 200 iterations, incorporating the 3D axial probe and the 1D support, to generate an enhanced 3D reconstruction. The axial-probe model used here is distinct from the position-dependent defocus correction applied during ptychographic reconstruction. The defocus correction accounts for the gradual change in specimen height across each tilted 2D scan, whereas the axial probe models how the convergent electron beam changes with depth within the 3D specimen. Spatial alignment and angular refinement were then conducted by aligning the experimental projections with the calculated projections (Supplementary Fig. 5). Finally, a third RESIRE cycle consisting of 200 iterations, incorporating both the axial probe and the 1D support, was performed to obtain the refined 3D reconstruction. The reconstruction assumes a single static structure that best fits all 13 projections. An additional Si-associated vacancy-like feature was visible only in projections 5–9 and was therefore not classified as a persistent vacancy in the final model. Resolving such transient structural changes would require time-resolved 3D atomic reconstruction. For each tilt, we calculated the R-factor between the experimental projection and the corresponding projection from the 3D reconstruction. The 13 values are 11.9%, 9.3%, 12.5%, 13.5%, 11.0%, 12.7%, 10.1%, 9.9%, 12.2%, 11.1%, 14.4%, 10.1% and 9.7%, with a mean of 11.4%.

Iterative atom tracing from the final tomographic reconstruction

To address the limited number of projections and the presence of a large missing wedge, we developed an iterative atom-tracing method to identify the 3D atomic coordinates from the final tomographic reconstruction. Supplementary Fig. 8a shows a diagram of the method, which began tracing atoms from the final reconstruction using the polynomial method[24,26,58], while enforcing a minimum nearest-neighbour distance of 1.35 Å. After examining all the local maxima, a set of 3D coordinates for the initial atoms was obtained, from which an average initial atom with dimensions of 2.19 × 2.19 × 2.19 Å^3 was calculated. At each traced position, the average initial atom was subtracted from the final reconstruction, and the polynomial method was then applied to the residual volume to identify additional atoms and generate an average residual atom. This average residual atom, along with the traced residual atom positions, was used for the next iteration. At each iteration, an R_1 factor was calculated, defined as the difference between the calculated and experimental projections[24]. The calculated projections were derived from a 3D structure in which all traced atom positions were filled with an average atom. Compared to previous non-iterative atom-tracing approaches[24–26], the current method refines atom positions by iterating between initial and residual atoms. Supplementary Fig. 8b shows the decrease in the R_1 factor as the iteration number increases, with the process terminating after ten iterations. Because not all atoms were initially identified, the intermediate reconstruction was corrected by subtracting an average atomic density at the traced atom positions from the tenth iteration, followed by additional tracing using the polynomial method. The iterative automated tracing algorithm successfully identified approximately 93% of the atoms. The remaining atoms were located through manual inspection followed by quantitative fitting. Specifically, manual inspection was used only to identify visible local maxima that were missed by the automated peak-search algorithm because of local intensity variations, peak overlap or background fluctuations. A 3D Gaussian function was then fitted to each identified local maximum to determine the centroids of the remaining ~7% of atoms using the same procedure applied to the automatically traced atoms. In total, 6,648 carbon atoms and 3 silicon atoms were identified.

Refining the 3D atomic coordinates

The traced 3D atomic coordinates were refined by minimizing the error between the calculated and experimental images using gradient descent. Specifically, each atom was modelled as a 3D Gaussian function to generate a 3D atomic model[24],

$$O'\{x,y,z\} = \sum_i H_i \exp\left(-\frac{|x-x_i|^2 + |y-y_i|^2 + |z-z_i|^2}{B'_i}\right) \quad (3)$$

where x_i, y_i and z_i represent the coordinates of the ith atom, H_i is the scaling factor, and B'_i describes the effective atomic-profile width, including finite spatial resolution, thermal motion and residual experimental broadening. The fitted 3D atomic model was then linearly projected to generate images using the experimental tilt angles. To improve precision, positional and angular refinement was performed using the 3D atomic model. For each experimental projection, a series of calculated projections was generated from the model over a range of tilt angles centred on the experimentally calibrated values. The tilt angles were then refined by maximizing the cross-correlation between the calculated and experimental projections. This process was iteratively repeated until no further improvement was detected, yielding a refined set of atomic positions and optimized tilt angles for the experimental projections. The final R_1 factor of the atom refinement process is 12%. To eliminate edge effects, atoms located at the boundary of the atomic model were excluded from the position refinement.

3D precision estimation

Multislice ptychographic datasets for precision estimation were simulated in abTEM[59] from the experimental 3D atomic model using the refined tilt angles and parameters listed in Extended Data Table 1. Thermal motion was represented by 64 frozen-phonon configurations, and Poisson noise corresponding to the experimental dose was added. Each tilt dataset was reconstructed using multimode ePIE[40,41], and the resulting phase projection was convolved with an optimized Gaussian kernel to reproduce the experimental broadening. The simulated projections were then processed using the same RESIRE reconstruction, atom-tracing and coordinate-refinement workflow as the experimental data. The resulting precision estimates are reported in the main text and Extended Data Fig. 3.

To obtain a more rigorous precision estimate, we independently displaced each atom in the DFT-relaxed TBG model by a random amount between −10 and +10 pm along each of the x, y and z axes. We then generated multislice ptychographic datasets using the same tilt geometry and imaging parameters as in the experiment, including 32 frozen-phonon configurations to model thermal vibrations and Poisson noise at the experimental dose. The simulated data were processed through the same pAET workflow used for the experimental data, including ptychographic reconstruction, tomographic reconstruction with a z-support constraint, iterative atom tracing and position refinement. Comparison of the reconstructed and known ground-truth coordinates yielded RMSDs of 4, 5 and 8 pm along x, y and z, respectively, and an overall 3D RMSD of 10 pm (Supplementary Fig. 9).

To complement the simulation-based precision estimates, we also evaluated coordinate reproducibility directly from the experimental data using two independent reconstructions with altered reconstruction constraints, as described in the main text. Replacing the generalized Gaussian z-support with transient square supports yielded a 3D RMSD of 8 pm, while reconstruction and refinement without either

the 1D z-support or axial probe yielded a 3D RMSD of 12 pm relative to the full pAET model (Extended Data Fig. 4 and Supplementary Fig. 10).

Determination of 3D atomic displacement vectors

To calculate atomic displacement vectors in TBG, we first created an unrelaxed TBG model consisting of two flat graphene layers with an interlayer distance of 3.43 Å, consistent with the mean interlayer distance observed in the experiment. The atomic displacement vectors were then determined by calculating the differences in atomic positions between the experimental model and the rigid model. To enhance the statistical precision of the displacement vector field, the atomic positions were convolved with 3D Gaussian kernels. This smoothing suppresses high-frequency noise and local fluctuations, enabling more robust extraction of long-wavelength structural distortions. Two kernel sizes were applied: one with standard deviations equal to half the lattice constant in the xy plane ($\sigma_x = \sigma_y = 1.26$ Å) and half the mean interlayer distance along z ($\sigma_z = 1.71$ Å), and another with standard deviations equal to the full lattice constant in the xy plane and the full interlayer distance along z.

Figure 4 shows the 3D displacement vectors and chiral lattice distortions in the experimental TBG structure after convolution with the larger Gaussian kernel. For comparison, Extended Data Fig. 6 shows the same analysis using the smaller kernel. Although convolution with the larger kernel reduces local fluctuations and produces a smoother displacement field, the key features of the 3D displacement vectors and chiral lattice distortions remain consistent between the two analyses. To test the robustness of the observed displacement fields, we performed multislice simulations of a flat-bilayer graphene model with a 1.96° twist angle and an interlayer spacing of 3.43 Å. The simulated diffraction patterns were processed using the same pAET pipeline (Extended Data Fig. 1) applied to the experimental data, yielding a reconstructed atomic model. After convolving this model with both Gaussian kernels, no spurious structural textures were observed, confirming that the observed chiral distortions in the experimental data are intrinsic and not artifacts of the analysis procedure.

Calculation of the skyrmion number

To compute the skyrmion number, we normalized the displacement vectors, triangulated the TBG lattices and calculated the solid angle (Ω) of each triangular surface subtended by three normalized vectors ($\mathbf{n}_1$, $\mathbf{n}_2$ and $\mathbf{n}_3$). The solid angle is given by[60,61]

$$\tan\frac{\Omega}{2} = \frac{\mathbf{n}_1 \cdot (\mathbf{n}_2 \times \mathbf{n}_3)}{1 + \mathbf{n}_1 \cdot \mathbf{n}_2 + \mathbf{n}_1 \cdot \mathbf{n}_3 + \mathbf{n}_2 \cdot \mathbf{n}_3}. \quad (4)$$

The skyrmion number was calculated by summing the solid angles over all consistently oriented triangles within the selected region and dividing by 4π,

$$N_s = \frac{1}{4\pi} \sum_{\text{all triangles}} \Omega \quad (5)$$

DFT calculations of relaxed and experimental 3D atomic models of a moiré supercell

A moiré supercell of TBG was constructed using the following approach. Let $\mathbf{a}_i$ for $i = 1, 2$ represent the lattice vectors that define the primitive cell of the top layer in the TBG. The lattice vectors of the bottom layer are given by $\mathbf{b}_i = R(\theta)\,\mathbf{a}_i$, where $R(\theta)$ is the rotation matrix and θ is the twist angle. The lattice vectors of the moiré supercell are defined as, $\mathbf{L}_1 = m\mathbf{a}_1 + n\mathbf{a}_2$ and $\mathbf{L}_2 = -R\left(\frac{\pi}{3}\right)\mathbf{L}_1$, where m and n are integers. The twist angle θ and the lattice constant L of the moiré supercell can be expressed in terms of the integers m and n,

$$\cos\theta = \frac{m^2 + n^2 + 4mn}{2(m^2 + n^2 + mn)}, L = |\mathbf{L}_1| = |\mathbf{L}_2| = \frac{a|m - n|}{2\sin\left(\frac{\theta}{2}\right)}, \quad (6)$$

where $a = |\mathbf{a}_1| = |\mathbf{a}_2|$ is the lattice constant of the primitive cell[62]. When L equals the moiré pattern period $L_m = \frac{a}{2\sin\left(\frac{\theta}{2}\right)}$, the condition $n - m = 1$ holds. A twist angle $\theta = 2.005°$ corresponds to the pair $(n, m) = (17, 16)$. Under this condition, the superlattice constant $L = 7.01$ nm, which is consistent with the measured moiré pattern period of approximately 7 nm. After determining the values of n and m, the TBG moiré supercell can be constructed, comprising 3,268 atoms. The supercell dimension along the z axis was set to 12 Å, which is sufficient for convergence according to prior benchmarks[63].

The constructed TBG moiré supercell was structurally relaxed using the Vienna Ab initio Simulation Package[64]. The rev-vdW-DF2 exchange–correlation functional was used to describe nonlocal van der Waals interactions[65], following its previous application to the structural relaxation and corrugation of TBG[63]. A plane-wave kinetic-energy cutoff of 420 eV was used. The electronic self-consistency criterion was set to 1.0×10^{-4} eV, and ionic relaxation was continued until the magnitude of the residual force on every atom was below 1.0×10^{-2} eV Å^{-1}. This force threshold served solely as the numerical convergence criterion for structural relaxation and was not interpreted as an atomic-position uncertainty. Brillouin-zone integrations were performed using a Γ-centred $2 \times 2 \times 1$ k-point mesh. A calculation using a $1 \times 1 \times 1$ mesh yielded a similar charge density, providing a consistency check on the electron-density distribution. The electronic band structure was calculated along the high-symmetry path Γ–M–K–Γ, using five k-points along each segment.

To derive the electronic band structure from the experimental data, we constructed a moiré supercell using the experimentally measured 3D atomic coordinates of TBG, comprising 3,267 carbon atoms and one silicon atom. Because band-structure calculations require periodic boundary conditions, only atoms near the supercell boundary were matched to the corresponding relaxed coordinates to ensure periodic continuity, while the Gaussian-smoothed experimental coordinates were retained throughout the interior. Because the experimental structure was not relaxed, we evaluated the residual forces on the Gaussian-smoothed, boundary-conditioned coordinates. The root-mean-square force components were 0.96, 0.89 and 0.04 eV Å^{-1} along x, y and z, respectively, while the corresponding mean components were close to zero, indicating no net directional force. Using a graphene C–C bond-stretching force constant of 7.174 mdyn Å^{-1} (ref. 66), equivalent to approximately 44.8 eV Å^{-2}, an in-plane force of approximately 0.9 eV Å^{-1} corresponds, as an order-of-magnitude estimate, to a bond-length change of approximately 0.02 Å. The much smaller z-direction root-mean-square force and its near-zero mean indicate no net out-of-plane force bias. The band structure of the experimental TBG was then calculated along the high-symmetry path Γ–M-K–Γ within the first Brillouin zone, using the same potential and exchange–correlation functional as in the relaxed model.

Comparison of the full-supercell DFT calculations for the relaxed and experimentally determined 3D atomic models indicates that the measured sample-specific geometry, including corrugation, stacking registry and local strain, modifies the electronic structure of TBG (Fig. 5). Because both models were evaluated using the same computational framework, the relative changes in band asymmetry and bandwidth are more informative than the absolute gap value. The calculated 22-meV gap should therefore be interpreted as a sample-specific result for the Gaussian-smoothed, boundary-conditioned experimental structure. Its magnitude may depend on the exchange–correlation functional and on the omission of quasiparticle and other many-body corrections.

Multislice pAET simulations of a diamond nanocrystal containing an NV centre

A 3D atomic model of a diamond nanocrystal was constructed with $12 \times 12 \times 43$ unit cells. To create an NV centre, one carbon atom was removed from the central unit cell, and a neighbouring carbon site was

replaced with a substitutional nitrogen atom. The atomic coordinates of the 3 × 3 × 3 unit cells surrounding the NV centre were relaxed using Vienna Ab initio Simulation Package[64], using the local-density approximation and the projector-augmented-wave method[67,68]. The 3D atomic coordinates were used as input to abTEM[59] to generate ptychographic datasets with the following parameters: accelerating voltage of 70 kV, convergence semi-angle of 32 mrad, collection angle of 70 mrad, 84 × 84 pixels per diffraction pattern, and a scan step size of 0.4 Å (Extended Data Table 1). To account for thermal diffuse scattering observed in experiments, diffraction patterns were simulated using 16 frozen phonons for the projected potential. Poisson noise was added to the diffraction patterns to simulate an electron dose of 1.0×10^4 e^- Å^{-2} per projection. Due to the 15-nm thickness of the diamond nanocrystal, a large angular tilt range was required to achieve an accurate tomographic reconstruction. A total of 57 tilt angles, ranging from −70° to 70° in 2.5° increments, were used to simulate ptychographic data along a single tilt axis.

Single- and multislice ptychographic reconstructions were performed using a maximum likelihood algorithm implemented in fold-slice, a MATLAB package adapted from Ptychoshelves[69–71]. Unlike ePIE[40], fold-slice includes a regularization term on the object function that suppresses unphysical phase fluctuations along the depth, thereby enhancing the stability of multislice ptychographic reconstructions[17,18,70,71]. This algorithm improves noise tolerance and enhances reconstruction accuracy, particularly in datasets with limited redundancy. Diffraction patterns were padded from 84×84 to 128×128 pixels prior to reconstruction to achieve a real-space pixel size of 0.213 Å. Each reconstruction was performed with 200 iterations using a single probe mode. The optimization step sizes for both the object and probes were set to 0.1. In the multislice ptychographic reconstruction, the object function was divided into 20 slices, each 1 nm thick, with a regularization factor of 0.5.

Using two sets of 57 projections obtained through single- and multislice ptychography, we conducted tomographic reconstructions with and without incorporating the axial probe. Extended Data Fig. 8a–d illustrates the 3D atomic structure around the NV centre, reconstructed using single-slice ptychography without and with probe incorporation. Due to the diamond nanocrystal's thickness being approximately three times the depth of focus of the electron probe, pAET reconstructions based on single-slice ptychography were unable to resolve individual atoms. However, multislice ptychography notably improves the pAET results. Extended Data Fig. 8e,f shows the 3D atomic structure of the NV centre in the *xy* and *xz* planes, reconstructed by multislice pAET without probe incorporation. These results appear less well defined than the reconstruction with probe incorporation (Extended Data Fig. 8g,h), where carbon atoms and the vacancy are more distinctly resolved (Extended Data Fig. 8i). Quantitatively, multislice pAET with probe incorporation yields the highest localization precision, with an RMSD of 7 pm, which is 2 pm better than that obtained without probe integration (Extended Data Fig. 8j). Despite this high precision, distinguishing nitrogen atoms from carbon atoms in diamond using pAET remains challenging, as it requires a higher electron dose owing to the minimal difference in atomic number ($\Delta Z = 1$).

Multislice pAET simulations of an amorphous carbon nanoparticle

A 3D atomic model of an amorphous carbon nanoparticle, 5 nm in diameter and containing 7,514 carbon atoms, was constructed. The structure was generated in LAMMPS using the Tersoff potential via a melt-quenching process[72], with a quenching rate of 0.3 K ps^{-1} to ensure high-quality amorphous configurations. The resulting 3D atomic coordinates were used as input for multislice ptychographic simulations performed with abTEM[59]. Simulation parameters included a 70 kV accelerating voltage, a probe with 13 nm underfocus, a convergence semi-angle of 32 mrad, a collection angle of 65 mrad, 128 × 128 pixels per diffraction pattern, and a scan step size of 0.65 Å (Extended Data Table 1). Eight frozen phonons were used to account for thermal diffuse scattering. Poisson noise was added to the simulated diffraction patterns to represent an electron dose of 1.5×10^4 e^- Å^{-2} per projection. Given the beam sensitivity of amorphous carbon, a wide angular range with relatively large tilt increments was used to balance reconstruction quality and radiation damage. Specifically, 37 tilt angles were simulated along a single axis, spanning from −72° to +72° in 4° steps, to generate the ptychographic dataset.

Multislice ptychographic reconstructions were carried out using a maximum likelihood algorithm implemented in fold-slice[69,70]. A representative reconstructed projection is shown in Extended Data Fig. 9a. The reconstruction framework includes a depth-resolution constraint governed by the combined effects of the probe's semi-convergence angle and the detector's maximum collection angle[14,15,18,71]. The real-space pixel size was 0.34 Å. Each reconstruction used a single probe mode and ran for 200 iterations, with step sizes of 0.02 applied to both the object and probe updates. The object volume was discretized into 10 slices of 1 nm thickness, and a regularization factor of 0.5 was applied during reconstruction.

After multislice ptychographic reconstruction at each angle, we applied tomographic reconstruction, atom tracing and position refinement, yielding a 3D atomic model of the amorphous nanoparticle (Extended Data Fig. 9b,c). Simulation and reconstruction parameters are summarized in Extended Data Table 1. Comparison with the ground-truth model yielded RMSDs of 4, 5, 9 and 11 pm along the *x*, *y* and *z* axes, and overall, respectively, with 99% of atoms correctly identified (Extended Data Fig. 9d–g). The medium-range order rings identified in the refined atomic model closely match those in the ground-truth structure (Extended Data Fig. 9h,i), validating the method's reliability in disordered systems. These results demonstrate that the pAET workflow developed in this study can achieve high-precision 3D atomic structure determination of amorphous carbon at experimentally relevant conditions.

Data availability

All experimental and simulated data supporting this paper are publicly available via GitHub at https://github.com/pAET-TBG/Supplementary-Data-Codes and via Zenodo at https://doi.org/10.5281/zenodo.17420338 (ref. 73).

Code availability

All source code supporting this Article, including code for ptychographic and tomographic reconstruction, atom tracing, position refinement and data analysis, is publicly available via GitHub at https://github.com/pAET-TBG/Supplementary-Data-Codes and via Zenodo at https://doi.org/10.5281/zenodo.17420338 (ref. 73).

References

53. Reina, A. et al. Large area, few-layer graphene films on arbitrary substrates by chemical vapor deposition. *Nano Lett.* **9**, 30–35 (2009).
54. Zobelli, A., Gloter, A., Ewels, C. P., Seifert, G. & Colliex, C. Electron knock-on cross section of carbon and boron nitride nanotubes. *Phys. Rev. B* **75**, 245402 (2007).
55. Meyer, J. C. et al. Accurate measurement of electron beam induced displacement cross sections for single-layer graphene. *Phys. Rev. Lett.* **108**, 196102 (2012).
56. Cao, S., Kok, P., Li, P., Maiden, A. M. & Rodenburg, J. M. Modal decomposition of a propagating matter wave via electron ptychography. *Phys. Rev. A* **94**, 063621 (2016).
57. Scott, M. C. et al. Electron tomography at 2.4-ångström resolution. *Nature* **483**, 444–447 (2012).
58. Rogers, S. S., Waigh, T. A., Zhao, X. & Lu, J. R. Precise particle tracking against a complicated background: polynomial fitting with Gaussian weight. *Phys. Biol.* **4**, 220–227 (2007).

59. Madsen, J. & Susi, T. The abTEM code: transmission electron microscopy from first principles. *Open Res. Eur.* **1**, 24 (2021).
60. Tserkovnyak, Y., Zou, J., Kim, S. K. & Takei, S. Quantum hydrodynamics of spin winding. *Phys. Rev. B* **102**, 224433 (2020).
61. Rana, A. et al. Three-dimensional topological magnetic monopoles and their interactions in a ferromagnetic meta-lattice. *Nat. Nanotechnol.* **18**, 227–232 (2023).
62. Uchida, K., Furuya, S., Iwata, J.-I. & Oshiyama, A. Atomic corrugation and electron localization due to moiré patterns in twisted bilayer graphenes. *Phys. Rev. B* **90**, 155451 (2014).
63. Lucignano, P., Alfè, D., Cataudella, V., Ninno, D. & Cantele, G. Crucial role of atomic corrugation on the flat bands and energy gaps of twisted bilayer graphene at the magic angle θ ~ 1.08°. *Phys. Rev. B* **99**, 195419 (2019).
64. Kresse, G. & Furthmüller, J. Efficient iterative schemes for ab initio total-energy calculations using a plane-wave basis set. *Phys. Rev. B* **54**, 11169–11186 (1996).
65. Hamada, I. van der Waals density functional made accurate. *Phys. Rev. B* **89**, 121103 (2014).
66. Medina, J. et al. Allowable stretching bond force constants on carbon nanomaterials: a DFT study. *Diam. Relat. Mater.* **126**, 109083 (2022).
67. Blöchl, P. E. Projector augmented-wave method. *Phys. Rev. B* **50**, 17953–17979 (1994).
68. Kresse, G. & Joubert, D. From ultrasoft pseudopotentials to the projector augmented-wave method. *Phys. Rev. B* **59**, 1758–1775 (1999).
69. Odstrčil, M., Menzel, A. & Guizar-Sicairos, M. Iterative least-squares solver for generalized maximum-likelihood ptychography. *Opt. Express* **26**, 3108–3123 (2018).
70. Wakonig, K. et al. PtychoShelves, a versatile high-level framework for high-performance analysis of ptychographic data. *J. Appl. Crystallogr.* **53**, 574–586 (2020).
71. Tsai, E. H. R., Usov, I., Diaz, A., Menzel, A. & Guizar-Sicairos, M. X-ray ptychography with extended depth of field. *Opt. Express* **24**, 29089–29108 (2016).
72. Tersoff, J. Empirical interatomic potential for carbon, with applications to amorphous carbon. *Phys. Rev. Lett.* **61**, 2879–2882 (1988).
73. Kim, N. Y. et al. Supplementary data codes. *Zenodo* https://doi.org/10.5281/zenodo.17420338 (2025).

Acknowledgements

We acknowledge J. C. Idrobo and A. R. Lupini for their assistance with the experiments, Y. Yang for help with data analysis, and M. Yoon and S. Yeom for discussions on DFT calculations.

Author contributions

J.M. directed the project. J.-H.P. and J.K. synthesized the graphene samples. N.Y.K., C.M.O., M.C. and J.M. discussed and/or conducted the experiments. J. Zhang, H.S., C.M.O., H.Z., N.Y.K., H.J. and J.M. contributed to the discussions and/or performed the ptychographic reconstructions. Y.Y., Y.L., M.P., H.Z. and J.M. developed and implemented the 3D axial probe kernel into tomographic reconstruction. H.Z., N.Y.K., C.M.O., Y.L., J.Zo., H.S., W.L., Y.Y., D.K. and J.M. performed the tomographic reconstructions, atom tracing, classification, data analysis and/or result interpretation. Y.L. conducted the DFT calculations. N.Y.K., C.M.O., H.Z., Y.L. and J.M. wrote the paper. All authors commented on the paper.

Funding

This research was primarily supported by the U.S. Department of Energy, Office of Science, Basic Energy Sciences, Division of Materials Sciences and Engineering, under award no. DE-SC0010378. N.Y.K., C.M.O., J.-H.P. and J.K. acknowledge support from the US Army Research Office MURI project under grant W911NF-18-1-0431. H.Z. acknowledges support from the US Air Force Office of Scientific Research MURI project under award no. FA9550-23-1-0281. M.C. acknowledges support from the US DOE, Office of Science, Basic Energy Sciences, Materials Sciences and Engineering Division. J. Zou acknowledges support from the Georg H. Endress Foundation. Electron ptychography and STEM experiments were conducted at the Center for Nanophase Materials Sciences at Oak Ridge National Laboratory which is a US-DOE Office of Science User Facility. Multislice simulations were performed at NERSC, a US Department of Energy Office of Science User Facility, under awards BES-ERCAP0028035 and ERCAP0034513.

Competing interests

The authors declare no competing interests.

Additional information

Extended data is available for this paper at https://doi.org/10.1038/s41565-026-02316-9.

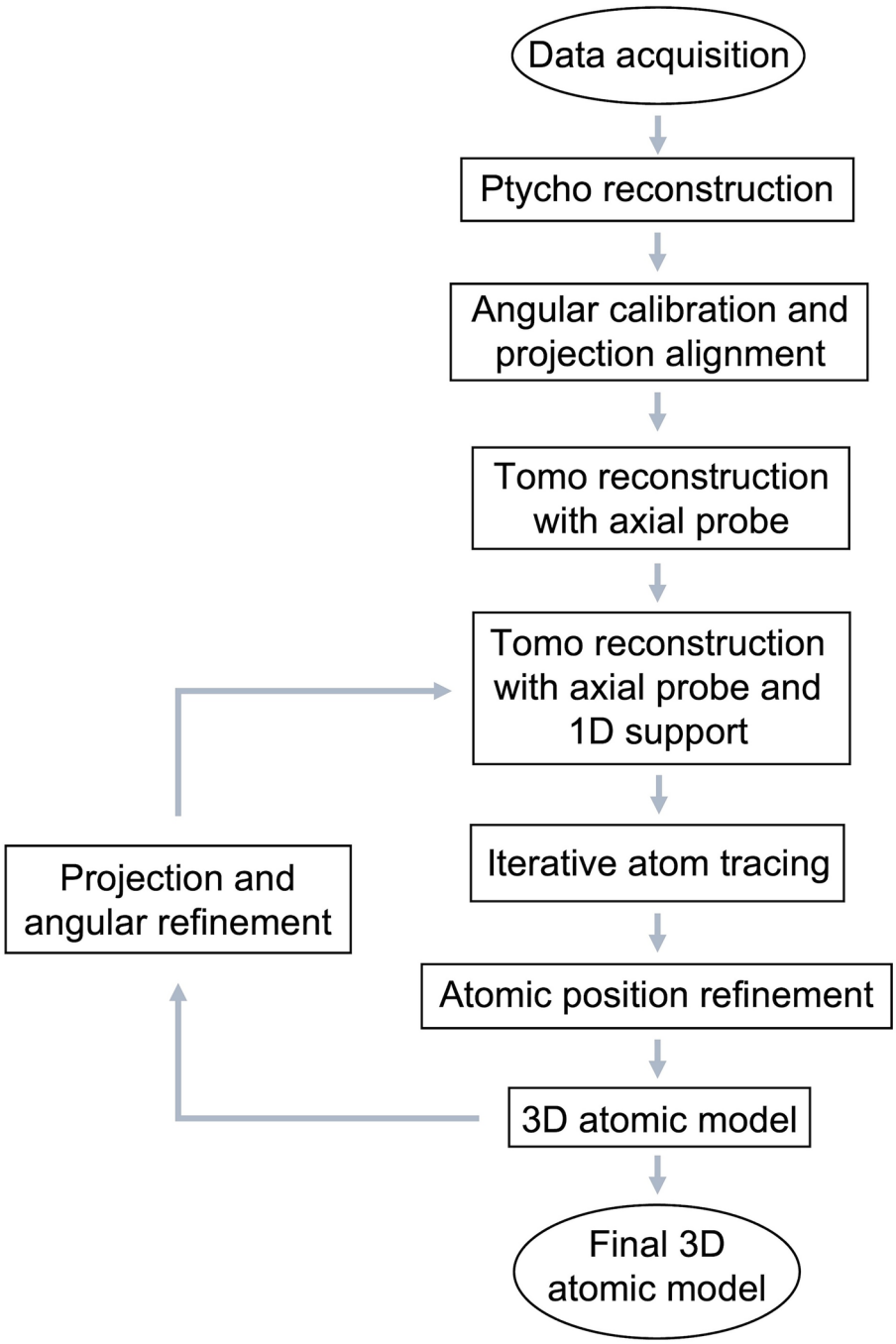
Supplementary information The online version contains supplementary material available at https://doi.org/10.1038/s41565-026-02316-9.

Correspondence and requests for materials should be addressed to Jianwei Miao.

Peer review information *Nature Nanotechnology* thanks Guoan Zheng and the other, anonymous, reviewer(s) for their contribution to the peer review of this work. Peer reviewer reports are available.

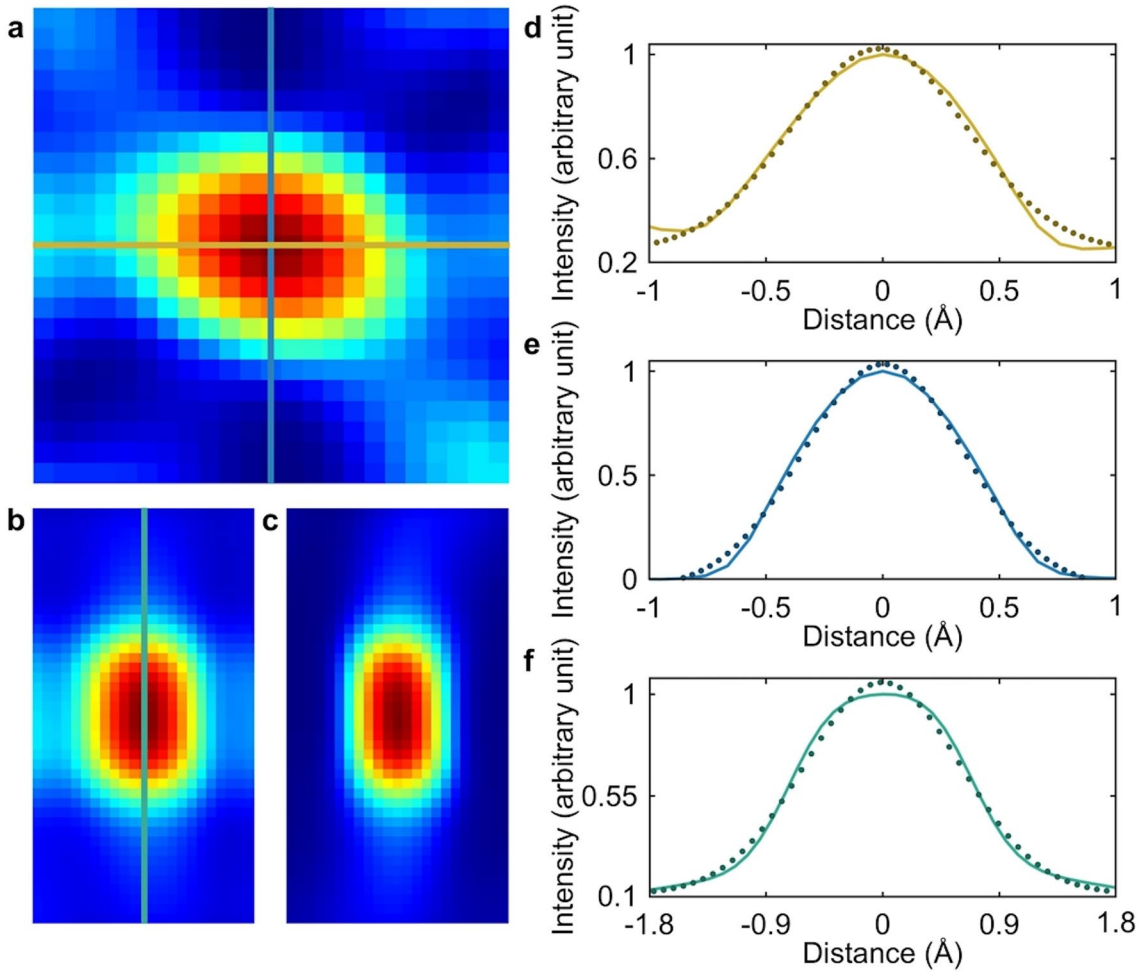
Reprints and permissions information is available at www.nature.com/reprints.

https://doi.org/10.1038/s41565-026-02316-9



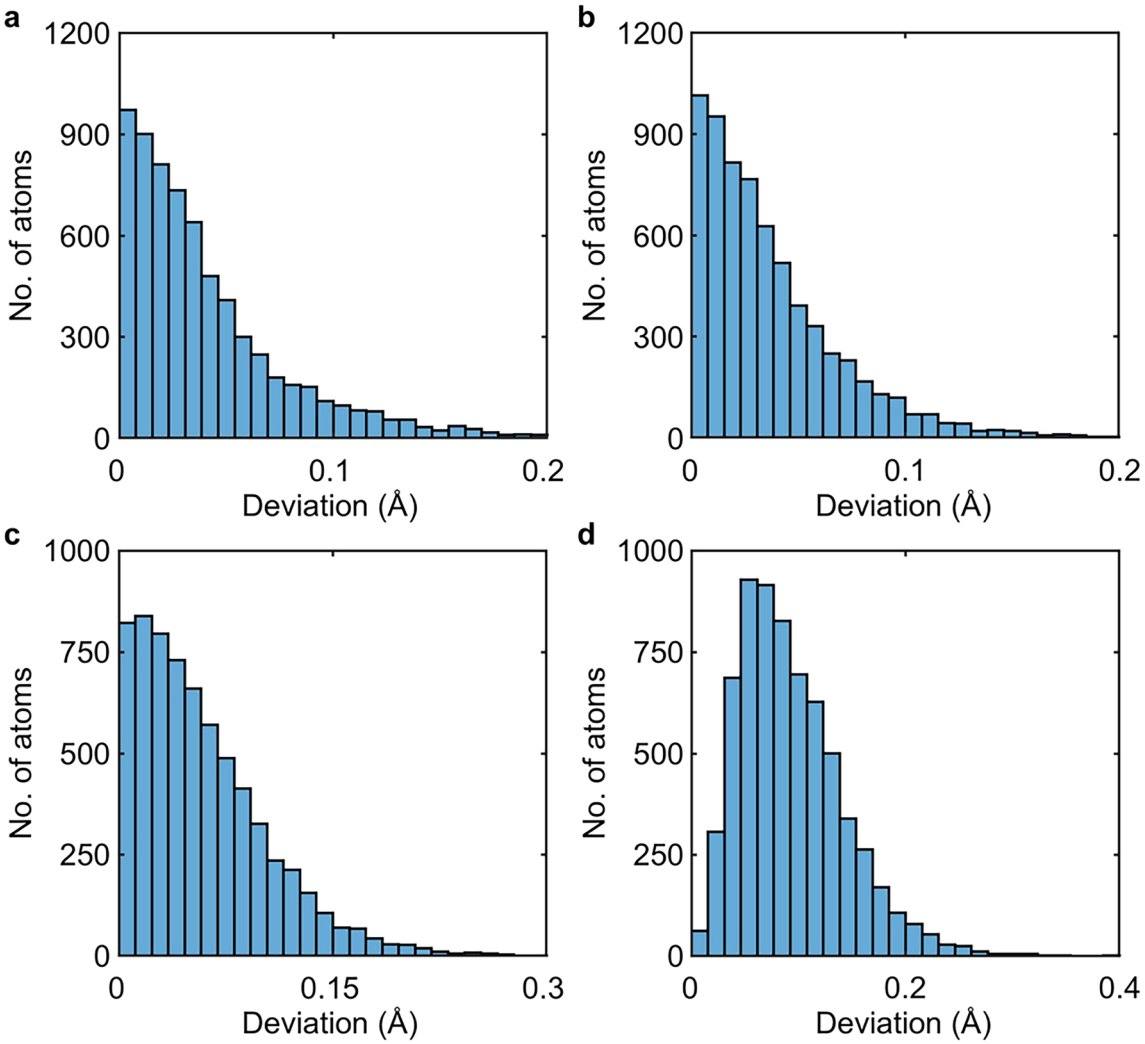
Extended Data Fig. 1 | Flowchart of the pAET pipeline. The workflow begins with data acquisition, followed by ptychographic reconstruction of the diffraction patterns to recover phase images. These phase projections are aligned through angular calibration and projection alignment. An initial tomographic reconstruction with an axial probe kernel retrieves 3D structural information, followed by another reconstruction with an axial probe and 1D z-support to enhance depth resolution. Iterative atom tracing identifies individual atomic positions, while atomic position and angular refinements further improve accuracy and consistency across tilts. The refined parameters are used for the final tomographic reconstruction with the axial probe and 1D z-support, followed by iterative atom tracing and refinement, yielding the final 3D atomic model.

https://doi.org/10.1038/s41565-026-02316-9



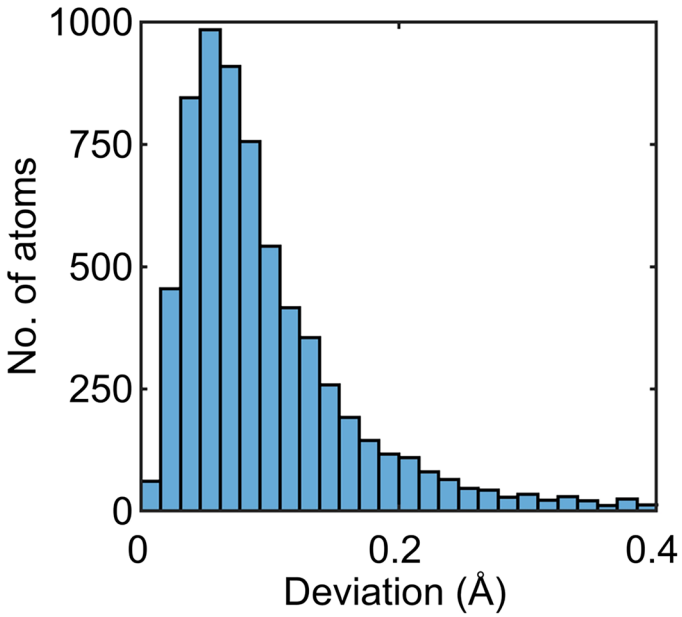
Extended Data Fig. 2 | Quantification of 3D spatial resolution with a 1D z-support constraint. a–**c**, Orthogonal *xy*, *xz*, and *yz* slices through the 3D atomic profile obtained by averaging subvolumes centred on 863 reconstructed carbon atoms. **d**–**f**, Corresponding 1D intensity profiles along *x*, *y*, and *z* through the centre of the averaged profile. Solid curves show the intensity profiles, and dotted curves show fits to a 1D Gaussian plus a constant background. The FWHMs of the fitted Gaussian peaks, measured relative to the fitted background, are 0.89, 0.82, and 1.42 Å along *x*, *y*, and *z*, respectively.

https://doi.org/10.1038/s41565-026-02316-9



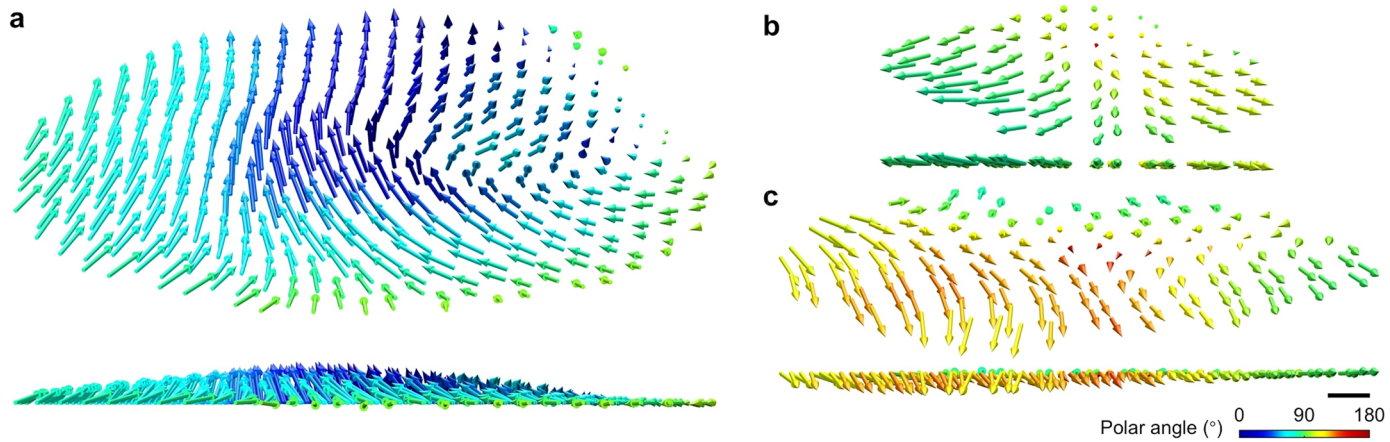
Extended Data Fig. 3 | Precision assessment of pAET using multislice simulations of the experimental 3D atomic model. a–d, Atomic-coordinate deviations between the input and reconstructed models along x, y, and z and in 3D, yielding RMSDs of 6, 5, 7, and 11 pm, respectively.

https://doi.org/10.1038/s41565-026-02316-9



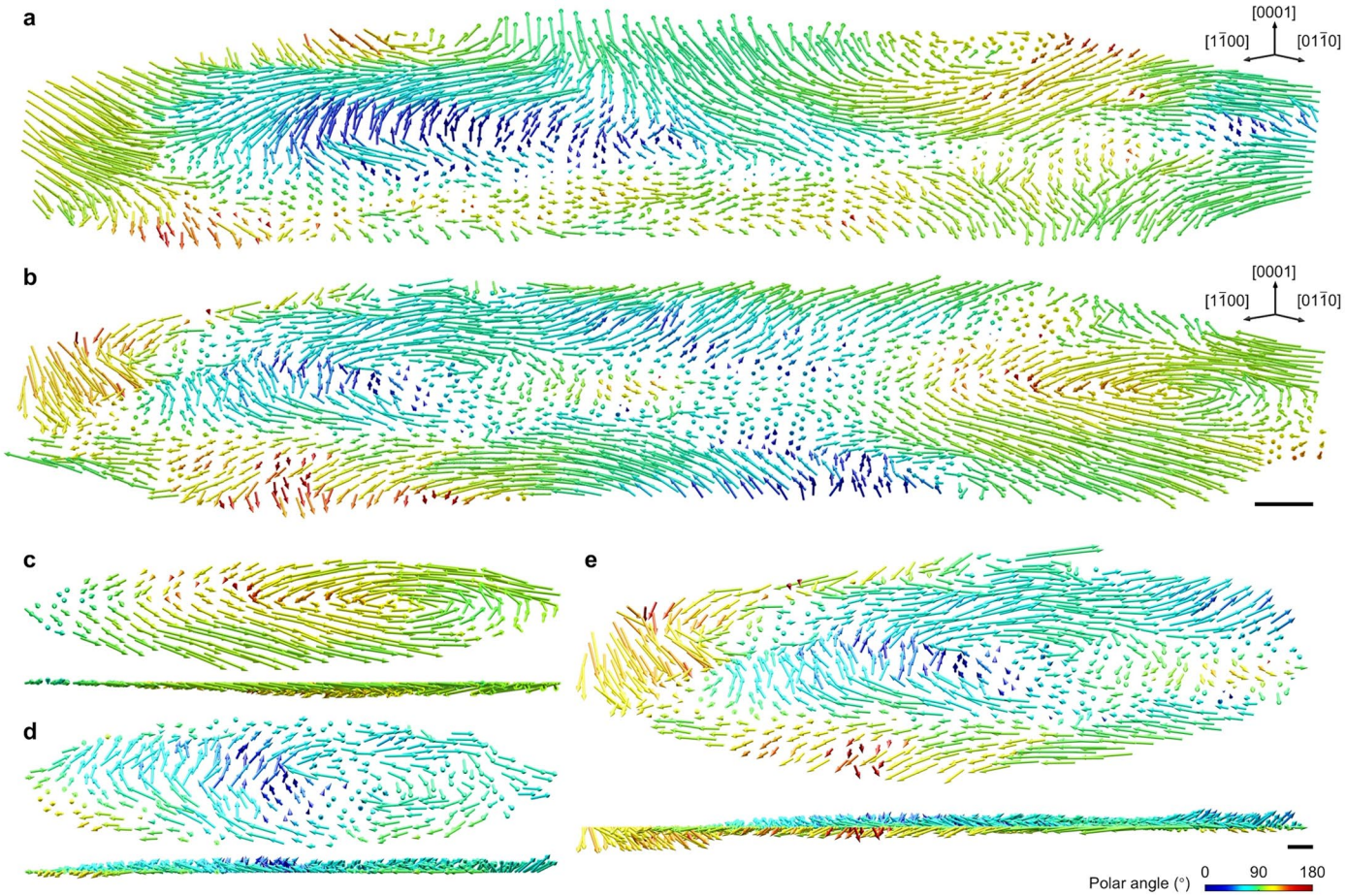
Extended Data Fig. 4 | Comparison of 3D atomic models obtained with and without reconstruction constraints. Histogram of 3D atomic-coordinate deviations between the model reconstructed and refined without either the 1D z-support or the axial-probe model and the model obtained using the full pAET workflow, yielding an overall RMSD of 12 pm.

https://doi.org/10.1038/s41565-026-02316-9



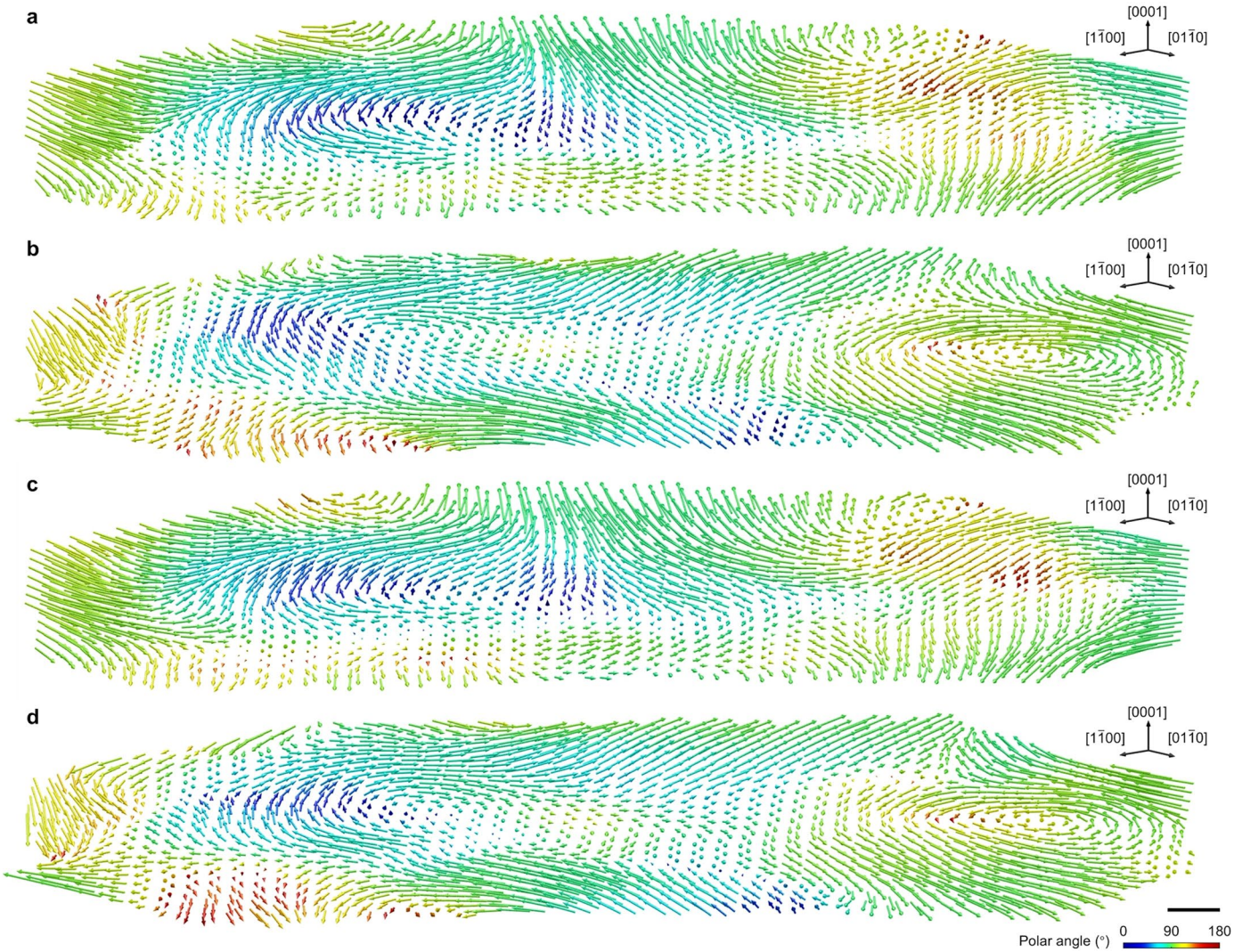
Extended Data Fig. 5 | Experimental 3D displacement vectors in TBG revealed by pAET. a–**c**, 3D vector fields of two anti-meron-like structural textures (**a**, **c**), with skyrmion numbers N_s = 0.35 and 0.45, respectively, and one meron-like structural texture (**b**), with N_s = −0.42. Vector colour represents the polar angle measured from the +z axis. To improve the precision of the displacement vector field at the expense of spatial resolution, atomic positions were convolved using a 3D Gaussian kernel with standard deviations equal to the in-plane lattice constant along x and y and the mean interlayer spacing along z. Displacement-vector lengths are enlarged 25-fold for visualization. Scale bar, 2 Å.

https://doi.org/10.1038/s41565-026-02316-9



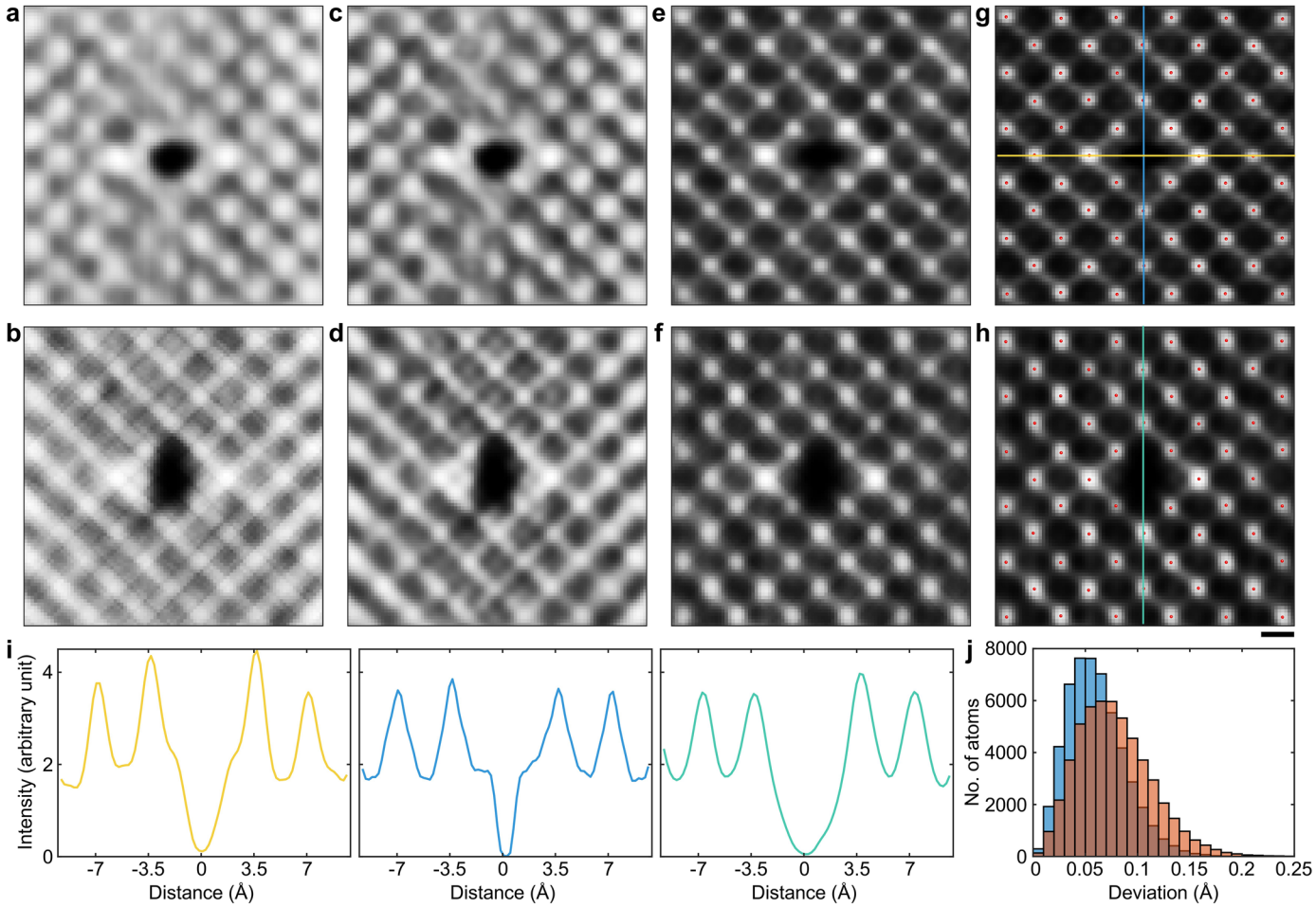
Extended Data Fig. 6 | 3D displacement vectors and chiral lattice distortions in experimental TBG. a, b, 3D displacement vectors in the top and bottom layers, with vector colour indicating the polar angle measured from the +z axis. **c**, **d**, Localized vector fields corresponding to a meron-like structural texture (**c**) and an anti-meron-like structural texture (**d**). **e**, 3D vector field of an anti-skyrmion-like structural texture. To improve displacement field precision at the expense of resolution, atomic positions were convolved using a 3D Gaussian kernel with standard deviations equal to half the in-plane lattice constant along x and y and half the mean interlayer spacing along z. Displacement-vector lengths are enlarged 25-fold for visualization. Scale bars, 5 Å in (**b**) and 2 Å in (**e**).

https://doi.org/10.1038/s41565-026-02316-9



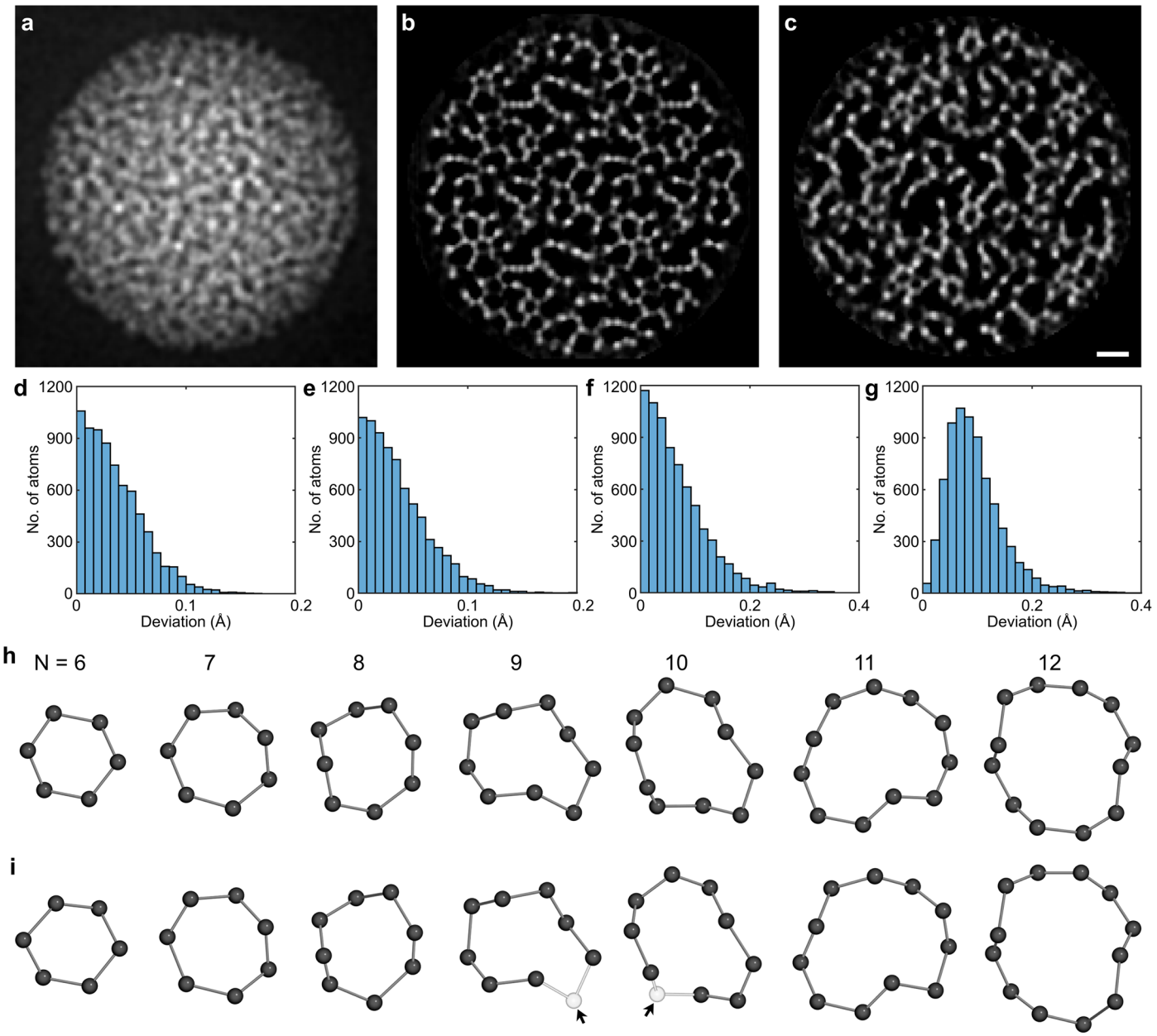
Extended Data Fig. 7 | Experimental 3D displacement vectors in TBG from split-half reconstructions. a, **b**, 3D displacement vector fields of the top and bottom graphene layers obtained from one split-half dataset. **c**, **d**, Corresponding 3D displacement vector fields of the top and bottom graphene layers obtained from the other split-half dataset. To improve displacement-field precision at the expense of spatial resolution, atomic positions were convolved using a 3D Gaussian kernel with standard deviations equal to the in-plane lattice constant along x and y and the mean interlayer spacing along z. Vector colour represents the polar angle measured from the +z axis. Displacement-vector lengths are enlarged 25-fold for visualization. Scale bar, 5 Å.

https://doi.org/10.1038/s41565-026-02316-9



Extended Data Fig. 8 | pAET simulations of an NV colour centre in diamond. **a**-**h**, 3D atomic structure of the NV centre in the xy (**a**, **c**, **e**, **g**) and xz (**b**, **d**, **f**, **h**) planes. Reconstructions were performed using pAET with single-slice ptychography without (**a**, **b**) and with probe incorporation (**c**, **d**), as well as multislice ptychography without (**e**, **f**) and with probe incorporation (**g**, **h**). Scale bar, 2 Å. **i**, Line scans along the x, y, and z directions around the NV centre, obtained using multislice pAET with probe incorporation, demonstrating high resolution. **j**, Histogram of deviations in 3D atomic positions. The 3D RMSDs obtained by multislice pAET with (blue) and without (orange) probe incorporation are 7 pm and 9 pm, respectively. Atom tracing from the single-slice reconstructions was unsuccessful, demonstrating the need for multislice ptychography for this specimen thickness.

https://doi.org/10.1038/s41565-026-02316-9



Extended Data Fig. 9 | 3D atomic-resolution pAET simulation of amorphous carbon. a, Ptychographic projection at 0°, reconstructed from electron diffraction patterns with a dose of 1.5×10^4 e^- $Å^{-2}$. **b**, **c**, Internal slices (1.3 Å thick) from the 3D reconstruction in the xy (**b**) and xz (**c**) planes, where the z axis corresponds to the missing wedge direction. Scale bar, 5 Å. **d**-**g**, Histograms of atomic-coordinate deviations between the reconstructed and ground-truth models along the x, y, and z axes and in 3D, yielding RMSDs of 4, 5, 9, and 11 pm, respectively. Overall, 99% of the atoms were correctly identified. **h**, Medium-range order motifs consisting of N-membered rings (N = 6-12) in the ground-truth atomic model. **i**, Corresponding ring structures in the reconstructed model, with arrows indicating two representative unidentified atoms within the displayed ring motifs.

https://doi.org/10.1038/s41565-026-02316-9

Extended Data Table 1 | Parameters for pAET data collection, reconstruction, and statistics

	TBG (Exp)	TBG (Sim)	NV centre in diamond (Sim)	Amorphous carbon nanoparticle (Sim)
Data Collection				
Voltage (kV)	70	70	70	70
Detector collection angle (mrad)	65	65	70	65
Convergence semi-angle (mrad)	32	32	32	32
Frozen phonon configurations	N/A	64	16	8
σ of Gaussian convolution (Å)	N/A	0.41	0.41	0.41
Scan step size (Å)	0.65	0.65	0.4	0.65
Number of scan positions	230×230	152×152	130×400	100×100
Number of projections	13	13	57	37
Pixel size (Å)	0.095	0.095	0.213	0.34
Tilt range	Supplementary Fig. 5b	Same as experiment	± 70° in 2.5° increments	± 72° in 4° increments
Electron dose per projection (e^- Å^{-2})	1.3×10^6	1.3×10^6	1.0×10^4	1.5×10^4
Defocus (nm)	0	0	0	+13
Ptychography				
Algorithm	Single-slice ePIE	Single-slice ePIE	Multislice Maximum likelihood	Multislice Maximum likelihood
Slice thickness (nm)	N/A	N/A	1	1
Number of probe modes	4	4	1	1
Number of iterations	100	100	200	200
Tomography reconstruction				
Algorithm	Improved RESIRE	Improved RESIRE	Improved RESIRE	Improved RESIRE
Number of iterations (final)	200	200	1,000	1,000
R (%)	11.4	8.3	2.0	1.6
Refinement				
B' factors (Å^2)				
C atoms	5.05	2.95	5.15	2.45
Si atoms	6.83	3.80	N/A	N/A
Number of atoms				
Total	6,651	6,652	52,530	7,514
C	6,648	6,649	52,529	7,514
Si	3	3	N/A	N/A
N	N/A	N/A	1*	N/A

*Distinguishing nitrogen atoms from carbon atoms in diamond with pAET requires a higher electron dose due to the minimal difference in their atomic numbers.

Experimental and simulated parameters for TBG, an NV centre in diamond and an amorphous carbon nanoparticle. Exp, experiment; Sim, simulation; ePIE, extended ptychographic iterative engine; RESIRE, real-space iterative reconstruction; N/A, not applicable.